

## Article

# The Influence of Speed Ratio on the Nonlinear Dynamics of a Magnetic Suspended Dual-Rotor System with a Fixed-Point Rubbing

Dongxiong Wang <sup>1,2</sup> , Songyao Chen <sup>1,2</sup>, Nianxian Wang <sup>3,4,\*</sup>, Ju Zhang <sup>1,2</sup> and Baohua Wang <sup>1,2</sup>

<sup>1</sup> School of Automotive Engineering, Hubei University of Automotive Technology, Shiyan 442002, China; ssrswdxiong@sina.com (D.W.)

<sup>2</sup> Hubei Key Laboratory of Automotive Power Train and Electronic Control, Shiyan 442002, China

<sup>3</sup> School of Machinery and Automation, Wuhan University of Science and Technology, Wuhan 430081, China

<sup>4</sup> Hubei Key Laboratory of Mechanical Transmission and Manufacturing Engineering, Wuhan University of Science and Technology, No. 947, Heping Venue, Qingshan District, Wuhan 430081, China

\* Correspondence: wangnianxian@wust.edu.cn

**Abstract:** Magnetic suspended dual-rotor systems (MSDS) provide the potential to significantly improve the performance of aero-engines by eliminating the wear and lubrication system, and solve vibration control issues effectively. However, the nonlinear dynamics of MSDS with rubbing is rarely investigated. In this work, the nonlinear support characteristics of active magnetic bearings (AMBs) are described by the equivalent magnetic circuit method, the impact force is characterized by the Lankarani–Nikravesh model, and the nonlinear dynamic model is established using the finite element method. On this basis, the influence of speed ratio on the nonlinear dynamics is investigated. Simulation results show that the fundamental sub-synchronous vibration of period  $n$  is the dominant motion of MSDS, where  $n$  is determined by the speed ratio. The frequency components of sub-synchronous vibrations of period  $k$  are integer multiples of the minimum dimensionless frequency component  $1/k$ , where  $k$  is a positive integral multiple of  $n$ . Quasi-periodic and chaotic vibrations are more likely to occur near critical speeds, and their main frequency components can be expressed as a variety of combined frequency components of the rotating frequency difference and its fractional frequency. To reduce the severity of fluctuating stresses stemming from complicated non-synchronous vibrations, speed ratios, corresponding to smaller  $n$  and AMB control parameters attenuating vibration amplitude or avoiding critical speeds, are suggested.

**Keywords:** speed ratio; fixed-point rubbing; magnetic suspended dual-rotor system; non-synchronous vibration



**Citation:** Wang, D.; Chen, S.; Wang, N.; Zhang, J.; Wang, B. The Influence of Speed Ratio on the Nonlinear Dynamics of a Magnetic Suspended Dual-Rotor System with a Fixed-Point Rubbing. *Actuators* **2023**, *12*, 354. <https://doi.org/10.3390/act12090354>

Received: 11 July 2023

Revised: 26 August 2023

Accepted: 3 September 2023

Published: 7 September 2023



**Copyright:** © 2023 by the authors. Licensee MDPI, Basel, Switzerland. This article is an open access article distributed under the terms and conditions of the Creative Commons Attribution (CC BY) license (<https://creativecommons.org/licenses/by/4.0/>).

## 1. Introduction

In order to obtain high efficiency and a high thrust-to-weight ratio, the dual-rotor structure is widely adopted as the core rotor component of aero-engines. In virtue of advantages like no mechanical friction, no wear, no lubrication, high speed and the long life of active magnetic bearings (AMBs), the substitution of AMBs for mechanical bearings to support a dual-rotor system constitutes the magnetic suspended dual-rotor system (MSDS), which can achieve significant reduction in system complexity and weight, structure optimization, and improvement in system reliability, maintainability and overall performance, in addition to being an effective solution to vibration control issues [1].

Reducing clearance between rotating and stationary components brings many benefits, such as a sharp decrease in specific fuel consumption, compressor stall margin and engine efficiency as well as increased payload and mission range capabilities [2]. At the same time, it also increases the possibility of rub impact. Rub impact is a typical fault in rotating machinery, and it may result in violent structural vibration, severe seal wear, increased

noise, or even catastrophic accidents. Therefore, the investigation of MSDS' rubbing characteristics is of great concern to the stability and security of actual aero-engines.

In the last decade, extensive attention was focused on the rubbing faults between rotating and stationary parts of dual-rotor systems in aero-engines. Since multi-frequency excitation of inner and outer rotors and complicated coupling characteristics induced by inter-shaft bearings concurrently exist in dual-rotor systems, the influence of rubbing on their dynamic behaviors is more complicated. Taking blade-casing rubbing, nonlinear characteristics of bearings and misalignment between dual-rotor structures and couplings into consideration, Jin et al. [3] explored the fault response characteristics of blade-casing rubbing. Yu et al. [4,5] developed a modal analysis method of aero-engine rotors under rub impact and investigated the nonlinear modal of a dual-rotor system and its effect on rotor vibration. Ling et al. [6] derived a rub impact force model between inner and outer shafts in a dual-rotor system, established a dynamic model of rub impact based on the solid finite element method, and analyzed the dynamic characteristics of a dual-rotor system caused by rub impact between shafts. With the Lankarani–Nikravesh model describing the impact force, Yang et al. [2,7] analyzed the influence of speed ratio, initial clearance and radius of curvature of limiters on the dynamic responses under fixed-point rubbing. Wang et al. [8] discussed the influence of speed ratio, unbalance and contact stiffness on rubbing fault between rotor blades and a casing, and found that the fractional frequency components of the rotational speed difference of inner and outer rotors were stimulated near the impact frequency and its multiple frequency components. In addition, some scholars studied the nonlinear dynamics of dual-rotor systems under rubbing faults. Chen et al. [9] presented a modified harmonic balance-alternating frequency/time domain method to analyze the nonlinear dynamics of a dual-rotor-bearing-casing system, and determined nonlinear dynamic behaviors such as vibration jumping and bi-stable and resonance hysteresis. Zhang et al. [10] investigated the spectral characteristics and bifurcation behaviors of a dual-rotor system and observed that both torsional vibration and bending vibration were portrayed by similar characteristic frequencies like fractional frequency, multiple frequency and the combined frequency of working and multiple frequency, or fractional frequency. The above-mentioned research not only considered the complex structure of rotors and stators, but also described the change process and the form of rub impact more accurately. Furthermore, these publications mainly investigated dynamic modeling and dynamic characteristics with rub impact in dual-rotor systems supported by only mechanical bearings.

Research on the dynamic characteristics of MSDS has been conducted. Ebrahimi et al. [11,12] developed a dynamic model of a MSDS supported by two AMBs and two auxiliary bearings based on Lagrange equation, and explored the effects of some control parameters on the nonlinear dynamic characteristics. However, the potential rub impact fault between a dual-rotor system and casing was not incorporated into the dynamic model. The authors investigated the basic dynamic characteristics [13] and unbalance response characteristics [14,15] of the MSDS and explored the effects of AMB control parameters on the dynamic rubbing characteristics such as spectrum characteristics, rubbing trajectory, normal impact force, invading length and so on [16,17].

As is known, the speed ratio, defined as the ratio of rotational speed of the outer rotor to that of the inner rotor, is an important design parameter in dual-rotor systems. From the above research, it is shown that the speed ratio has a significant effect on the dynamic characteristics of dual-rotor systems. For example, when the speed ratio is close to 1, a beat vibration phenomenon occurs [2,7]. However, research on the nonlinear dynamic characteristics of MSDS under fixed-point rubbing faults requires consideration in the existing literature, and lacks insight into the bifurcation behavior and nonlinear motion characteristics of MSDS. Although the influence of speed ratio on fixed-point rubbing characteristics was analyzed in the previous literature, there is no systematic and comprehensive analysis of the influence of speed ratio on the nonlinear dynamic characteristics of MSDS, and the relationship between speed ratio and nonlinear periodic

motion has not been revealed. In fact, it is of crucial importance to perform such work for the safe and reliable operation and fault detection of MSDS.

In this research, considering the nonlinear support characteristics of AMBs and describing the impact force of fixed-point rubbing with the Lankarani–Nikravesh model, a rubbing dynamic model of MSDS is established with the finite element method and solved by the Newmark- $\beta$  method. On this basis, the influence of speed ratio on nonlinear dynamic rubbing characteristics are investigated by bifurcation diagrams, dynamic trajectories, Poincaré maps and spectrum graphs. In order to enhance the computational efficiency of bifurcation diagram generation, a parallel computing strategy is employed.

## 2. Mathematical Formulation

In this section, the governing equations of MSDS under a fixed-point rubbing fault are derived. The MSDS structure is depicted in Figure 1. It contains an inner rotor and an outer rotor, three disks, two AMBs and two inter-shaft bearings. The outer rotor and inner rotor are used to simulate the high-pressure shaft and low-pressure shaft in aero-engines, respectively. One end of the high-pressure shaft is connected to a high-pressure turbine and the other end is connected to a high-pressure compressor. One end of the low-pressure shaft is connected to a low-pressure turbine and the other end is connected to a low-pressure compressor after passing through the hollow high-pressure shaft. During the operation of aero-engines, sufficient air is introduced into the compressors through an intake port. The high-speed rotating compressors work on the air to produce high-pressure air. The high-pressure air is mixed with fuel in a combustion chamber to form high-temperature and high-pressure gas. The gas expands in the turbines to drive them to rotate, and continues to expand in a nozzle to make it eject at high speed to generate thrust. By effectively improving the volume utilization of the engine compression chamber, dual-rotor structures can achieve a higher efficiency and thrust-to-weight ratio than single-rotor systems. In addition, AMBs monitor and adjust the dynamic response of the outer rotor in real time through a feedback control system.

Due to neither extremely long or slender of the two rotor shafts, effects of torsion may be neglected, and later vibration is mainly focused in this work. Rubbing is supposed to occur between disk 3 and a fixed limiter. To facilitate analysis, the influence of thermal effect and friction torque during the rubbing process is neglected, and two eccentricities are, respectively, distributed on disk 1 and disk 3.

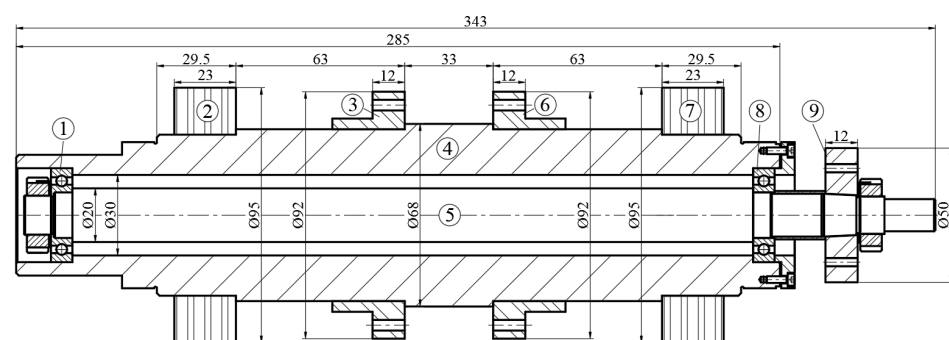


**Figure 1.** The MSDS Structure. 1, 8-Inter-shaft bearing, 2 and 7-AMB rotor, 3-Disk 2, 4-Outer rotor, 5-Inner rotor, 6-Disk 3, 9-Disk 1.

### 2.1. AMB Modeling

The model of AMB support characteristics is established by the equivalent magnetic circuit method. The structure of an eight-pole AMB in horizontal direction is illustrated in Figure 2a, where 1~4 represent the numbers of magnetic poles. Assuming that flux leakage,

magnetic saturation, and magnetic coupling are neglected, the equivalent magnetic circuit for a pole-pair is provided in Figure 2b. The magnetomotive forces  $M_1$  and  $M_2$  of coils are

$$M_1 = M_2 = \frac{N(I_b + I_x)}{2} \quad (1)$$

where,  $N$  is coil turn, and  $I_b$  and  $I_x$ , respectively, are the bias current and control current of the coils. The total reluctance  $R_t$  for the pole-pair is expressed as

$$R_t = R_{g1} + R_{g2} = \frac{g_1 + g_2}{\mu_0 A_p} \quad (2)$$

where,  $R_{g1}$  and  $R_{g2}$  are air gap reluctances,  $g_1$  and  $g_2$  are air gap lengths,  $\mu_0$  is permeability of vacuum, and  $A_p$  is the sectional area of a stator pole. As a result, the magnetic flux  $\Phi$  in a pole-pair is

$$\Phi = \frac{M_1 + M_2}{R_t} \quad (3)$$

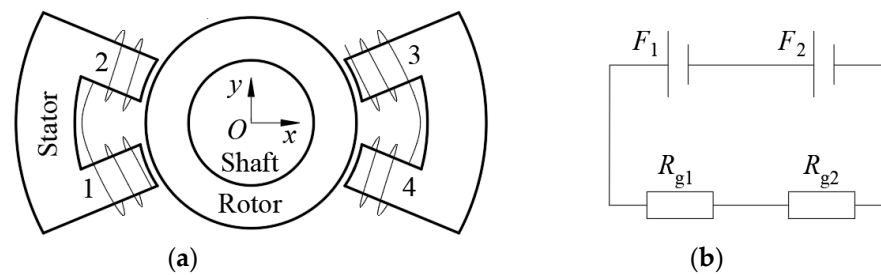


**Figure 2.** AMB configuration and the equivalent magnetic circuit for a pole-pair. (a) AMB structure in horizontal direction. (b) Equivalent magnetic circuit.

The electromagnetic force  $F_e$  produced by a pole-pair is expressed as

$$F_e = \frac{\Phi^2 \cos \varphi}{\mu_0 A_p} \quad (4)$$

where  $\varphi$  is the half angle between central lines of two adjacent poles. Therefore, for the AMB with a differential drive mode, the nonlinear electromagnetic force  $F_{ex}$  generated in the horizontal direction is

$$F_{ex} = \mu_0 N^2 A_p \cos \varphi \left[ \left( \frac{I_b + I_x}{g_3 + g_4} \right)^2 - \left( \frac{I_b - I_x}{g_1 + g_2} \right)^2 \right] \quad (5)$$

where  $g_3$  and  $g_4$  are air gap lengths between another pole-pair and the rotor in Figure 2. When the rotor center drifts to a position  $(x, y)$ , the four air gap lengths are expressed as

$$\begin{cases} g_1 = g_0 + x \cos \varphi + y \sin \varphi \\ g_2 = g_0 + x \cos \varphi - y \sin \varphi \\ g_3 = g_0 - x \cos \varphi - y \sin \varphi \\ g_4 = g_0 - x \cos \varphi + y \sin \varphi \end{cases} \quad (6)$$

Under PD control,  $I_x$  is given by

$$I_x = -K_p x - K_d \dot{x} \quad (7)$$

where,  $K_p$  and  $K_d$  are the proportional and derivative coefficients, respectively. Similarly, the nonlinear electromagnetic force  $F_{ey}$  in the vertical direction can be obtained.

### 2.2. Fixed-Point Rubbing Model

In actual aero-engines, there is a great possibility for the existence of convex points in vertical direction of a casing, resulting from thermal deformation or complicated external suspensions like pipelines and fuel tanks. Therefore, a fixed limiter is located in vertical direction to simulate a convex point, as shown in Figure 3. The Lankarani–Nikravesh model [2] is adopted to describe the impact force during a rubbing process. The friction force is assumed to obey the Coulomb law of friction. As a result, the normal impact force  $F_n$  and tangential friction force  $F_t$  are

$$\begin{cases} F_n = k_r h^{1.5} \left[ 1 + \frac{3(1-c_e^2)v}{4v_0} \right] \\ F_t = f_r F_n \end{cases} \quad (8)$$

where  $c_e$  and  $f_r$  are, respectively, the restitution coefficient and friction coefficient.  $h$  is the invading length of disk 3 in a collision direction.  $v$  and  $v_0$  are, respectively, the impact velocity of disk 3 and initial impact velocity during each rubbing process. The contact stiffness  $k_r$  is given as

$$k_r = \frac{4}{3 \left( \frac{1-\mu_d^2}{E_d} + \frac{1-\mu_p^2}{E_p} \right)} \left( \frac{R_d R_p}{R_d + R_p} \right)^{0.5} \quad (9)$$

where  $\mu_d, \mu_p, E_d, E_p, R_d$  and  $R_p$  are, respectively, the Poisson’s ratio, elastic modulus and radii of disk 3 and the limiter end.

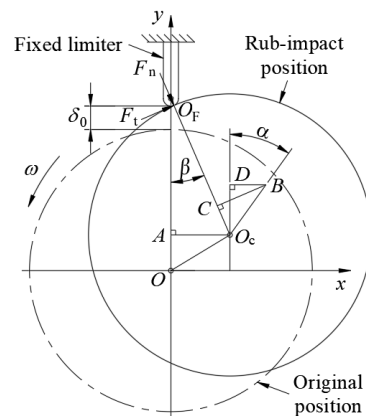


Figure 3. Rub impact force model for a disk-fixed limiter system.

According to the geometric relationship in Figure 3, the invading length  $h$  obeys

$$h = R_d + R_p - \sqrt{(R_d + R_p + \delta_0 - y)^2 + x^2} \quad (10)$$

where  $h > 0$  indicates the appearance of a collision. The contact angle  $\beta$  can be written as

$$\beta = \arctan \frac{x}{R_d + R_p + \delta_0 - y} \quad (11)$$

Thus,  $F_n$  and  $F_t$  can be calculated based on Equation (8), and their components in  $x$  and  $y$  are provided by

$$\begin{cases} F_{rx} = F_n \sin \beta + F_t \cos \beta \\ F_{ry} = -F_n \cos \beta + F_t \sin \beta \end{cases} \quad (12)$$

### 2.3. Dynamic Model under Fixed-Point Rubbing

As depicted in Figure 4, the dual-rotor structure is discretized into 40 segments and 35 nodes, and 1~35 in Figure 4 are the node numbers. The discretized model consists of 33 beam elements, 3 disk elements, 2 AMB support elements and 2 inter-shaft bearing support elements. The Euler–Bernoulli beam element is adopted to consider moment of inertia and gyroscopic effect. For convenient analysis, disk elements are assumed as rigid, and inter-shaft elements are modeled as linear springs and viscous dampers.

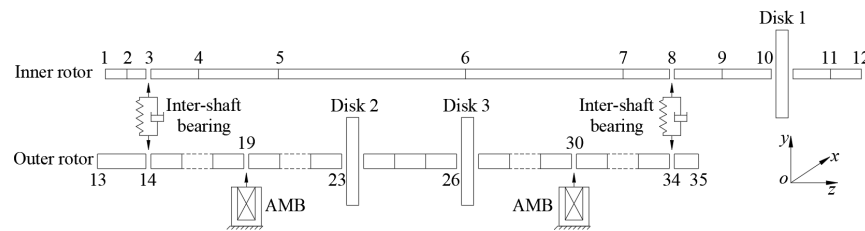


Figure 4. Finite element model of MSDS.

Based on the rotor dynamics theory, the governing equations of an inner rotor can be derived as

$$\begin{cases} M_i \ddot{q}_{1i} + \omega_i J_i \dot{q}_{2i} + K_i q_{1i} = F_{1i} \\ M_i \ddot{q}_{2i} - \omega_i J_i \dot{q}_{1i} + K_i q_{2i} = F_{2i} \end{cases} \quad (13)$$

where  $M_i$ ,  $J_i$  and  $K_i$ , respectively, represent mass, gyroscopic and stiffness matrices of the inner rotor. The detailed process of obtaining these matrix methods can be found in reference [2,7].  $\omega_i$  is the inner rotor rotational speed. The generalized displacement vectors of inner rotor  $q_{1i}$  and  $q_{2i}$  are written as

$$\begin{cases} q_{1i} = \{ x_1 \ \theta_{y1} \ x_2 \ \theta_{y2} \ \dots \ x_{12} \ \theta_{y12} \}^T \\ q_{2i} = \{ y_1 \ -\theta_{x1} \ x_2 \ -\theta_{x2} \ \dots \ x_{12} \ -\theta_{x12} \}^T \end{cases} \quad (14)$$

where  $x_k$  and  $y_k$  ( $k = 1, 2, \dots, 12$ ) are the translational displacement of nodes 1–12 and  $\theta_{yk}$ , and  $\theta_{xk}$  ( $k = 1, 2, \dots, 12$ ) are their angular displacement.  $F_{1i}$  and  $F_{2i}$  are the generalized force vectors, and they can be expressed as

$$\begin{cases} F_{1i} = \{ 0 \ 0 \ 0 \ \dots \ u_{d1} \omega_i^2 \cos(\omega_i t) \ 0 \ 0 \ 0 \ 0 \ 0 \ 0 \}^T \\ F_{2i} = \{ 0 \ 0 \ 0 \ \dots \ u_{d1} \omega_i^2 \sin(\omega_i t) \ 0 \ 0 \ 0 \ 0 \ 0 \ 0 \}^T \end{cases} \quad (15)$$

where  $u_{d1}$  is the imbalance on disk 1 and  $t$  is the time.

In the same way, the governing equations of an outer rotor are provided as

$$\begin{cases} M_o \ddot{q}_{1o} + \omega_o J_o \dot{q}_{2o} + K_o q_{1o} = F_{1o} \\ M_o \ddot{q}_{2o} - \omega_o J_o \dot{q}_{1o} + K_o q_{2o} = F_{2o} \end{cases} \quad (16)$$

$$\begin{cases} q_{1o} = \{ x_{13} \ \theta_{y13} \ x_{14} \ \theta_{y14} \ \dots \ x_{35} \ \theta_{y35} \}^T \\ q_{2o} = \{ y_{13} \ -\theta_{x13} \ x_{14} \ -\theta_{x14} \ \dots \ x_{35} \ -\theta_{x35} \}^T \end{cases} \quad (17)$$

$$\begin{cases} F_{1o} = \{ 0 \ 0 \ \dots \ F_{ex}^L \ 0 \ \dots \ u_{d3} \omega_o^2 \cos(\omega_o t) + F_{rx} \ 0 \ \dots \ F_{ex}^R \ 0 \ \dots \ 0 \ 0 \}^T \\ F_{2o} = \{ 0 \ 0 \ \dots \ F_{ey}^L \ 0 \ \dots \ u_{d3} \omega_o^2 \sin(\omega_o t) + F_{ry} \ 0 \ \dots \ F_{ey}^R \ 0 \ \dots \ 0 \ 0 \}^T \end{cases} \quad (18)$$

where  $F_{ex}^L$ ,  $F_{ey}^L$ ,  $F_{ex}^R$  and  $F_{ey}^R$  are the nonlinear electromagnetic forces of the left and right AMBs in horizontal and vertical directions, respectively. The other variables have the same physical meaning as Equations (13)–(15), and the subscript “o” of the variables represents the outer rotor.

Assembling the governing equations of these two rotor subsystems, the MSDS governing equations are derived as

$$\begin{bmatrix} M_i & 0 & 0 & 0 \\ 0 & M_o & 0 & 0 \\ 0 & 0 & M_i & 0 \\ 0 & 0 & 0 & M_o \end{bmatrix} \begin{Bmatrix} \ddot{q}_{1i} \\ \ddot{q}_{1o} \\ \ddot{q}_{2i} \\ \ddot{q}_{2o} \end{Bmatrix} + \begin{bmatrix} 0 & 0 & \omega_i J_i & 0 \\ 0 & 0 & 0 & \omega_o J_o \\ -\omega_i J_i & 0 & 0 & 0 \\ 0 & -\omega_o J_o & 0 & 0 \end{bmatrix} \begin{Bmatrix} \dot{q}_{1i} \\ \dot{q}_{1o} \\ \dot{q}_{2i} \\ \dot{q}_{2o} \end{Bmatrix} + \begin{bmatrix} K_i & 0 & 0 & 0 \\ 0 & K_o & 0 & 0 \\ 0 & 0 & K_i & 0 \\ 0 & 0 & 0 & K_o \end{bmatrix} \begin{Bmatrix} q_{1i} \\ q_{1o} \\ q_{2i} \\ q_{2o} \end{Bmatrix} = \begin{Bmatrix} F_{1i} \\ F_{1o} \\ F_{2i} \\ F_{2o} \end{Bmatrix} \quad (19)$$

In addition, the boundary conditions for the bearings, namely the stiffness and gyroscopic matrices in Equation (19), need to be handled. For simplicity, the specific modification details can be consulted in [2]. Eventually, the Newmark-β method is employed to obtain the solution of Equation (19).

2.4. Model validation

Based on the experimental results in [7], the validity of the MSDS dynamic model is verified. When the AMB works in a linear interval, the nonlinear factors have little effect on its support characteristics, and the dynamic responses of these two systems are essentially consistent [18]. Under this condition, AMB support characteristics can be linearized as equivalent stiffness and equivalent damping models [19]. The dual-rotor system [7] is shown in Figure 5, where 1~8 indicate the numbers of nodes. Applying the above modeling method to this dual-rotor system, with the equivalent stiffness and equivalent damping of AMBs, respectively, equivalent to those of mechanical bearings, the support characteristics of dual-rotor systems remains unchanged. The structural parameters of the dual-rotor system are consistent with those in reference [7], so they are not listed here.

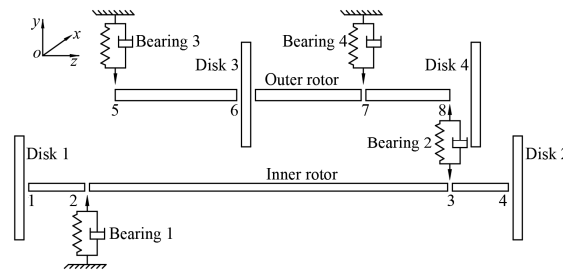


Figure 5. The model of dual-rotor system in [7].

When fixed-point rubbing occurs, the response spectra diagrams of the dual-rotor system are shown in Figure 6. It is shown that the response spectrum mainly includes the rotating frequencies  $\omega_i$  and  $\omega_o$  of inner and outer rotors as well as their combined frequency components  $\omega_o + \omega_i$  and  $2\omega_o$ . Hence, the simulation results are in good agreement with the experimental results. The variances of response amplitudes at these frequency components are caused by the differences in imbalance positions and initial conditions of the dual-rotor system. Therefore, the modeling method above is effective and the validity of the established dynamic model is verified.

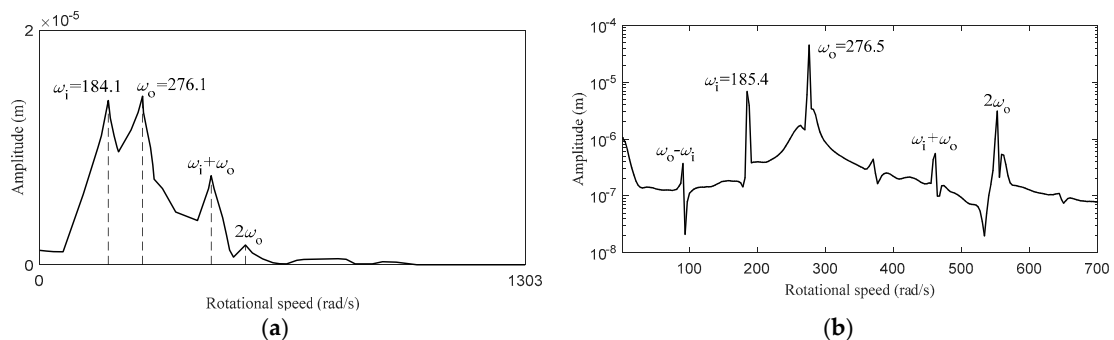


Figure 6. Response spectra diagrams of a dual-rotor system. (a) Experimental results in [7], (b) Simulation results.

### 3. Numerical Results and Discussion

Numerical integration is performed to explore the nonlinear dynamic characteristics of MSDS with fixed-point rubbing. The basic dimensions (unit, mm) of MSDS structure are depicted in Figure 1, and the other main parameters are listed in Table 1.

**Table 1.** Main parameters of MSDS.

Physical Parameter	Value	Physical Parameter	Value
Vacuum permeability $\mu_0$ (H/m)	$4\pi \times 10^7$	Inter-bearing damping $c_c$ (N·s/m)	0
Half angle between two poles $\varphi$ (°)	22.5	Radius of disk 3 $R_d$ (m)	0.046
Nominal air gap length $g_0$ (mm)	0.5	Radius of limiter end $R_p$ (m)	$1.25 \times 10^{-4}$
Sectional area of stator pole $A_p$ (mm <sup>2</sup> )	247	Poisson ratio of disk 3 $\mu_d$	0.3
Coil turn $N$	160	Poisson ratio of limiter $\mu_p$	0.3
Bias current $I_b$ (A)	3	Elastic modulus of disk 3 $E_d$ (Pa)	$2.09 \times 10^{11}$
Maximum control current $i_{cmax}$ (A)	3	Elastic modulus of limiter $E_p$ (Pa)	$2.09 \times 10^{11}$
Proportional coefficient $K_p$	5	Restitution coefficient $c_e$	0.9
Derivational coefficient $K_d$	$3 \times 10^{-4}$	Friction coefficient $f_r$	0.3
Initial rubbing clearance $\delta_0$ (m)	$1 \times 10^{-5}$	Imbalance of disk 1 $u_{d1}$ (Kg·m)	$3 \times 10^{-5}$
Inter-bearing stiffness $k_c$ (N/m)	$1 \times 10^7$	Imbalance of disk 3 $u_{d3}$ (Kg·m)	$3 \times 10^{-5}$

In a dual-rotor system, speed ratio is a basic and important parameter during the operation process, and it usually has a great influence on the dynamic response of dual-rotor systems. The speed ratio  $r$  is defined as the ratio of outer rotor speed  $\omega_o$  to inner rotor speed  $\omega_i$ , namely,  $r = \omega_o/\omega_i$ , and  $r > 0$  indicates a co-rotation, while  $r < 0$  indicates a counter-rotation. Generally, the values of speed ratio adopted in dual-rotor systems reported in literatures [2,8,11,12] change from 1 to 2 for the typical case of co-rotation. Hence, the values of speed ratio  $r$  fixed at 1.2, 1.3, 1.5 and 2.0 are selected to investigate their effects on MSDS responses. The rotating speed of the inner rotor is varied from 5 rad/s to 3000 rad/s at intervals of  $\Delta\omega_i = 5$  rad/s. For convenient analysis,  $\omega_i$  is normalized to the first order critical speed  $\omega_{cli}$  of MSDS excited by the inner rotor, the response displacements  $x$  and  $y$  are normalized to the AMB nominal air-gap length  $g_0$ , and the response frequency  $\omega$  is normalized to  $\omega_i$ , namely  $\Omega = \omega_i/\omega_{cli}$ ,  $X = x/g_0$  and  $Y = y/g_0$ , and  $N = \omega/\omega_i$ , respectively. For example, in the case of  $r = 1.2$ , control parameters  $K_p = 5$  and  $K_d = 0.0003$ , the first three order critical speeds calculated by complex Riccati transfer matrix method [13] are provided in Table 2. It is clear from Table 2 that  $r = 1.2$  is in co-rotation with  $\omega_{cli} = 828.48$  rad/s. Thus, a step of  $\Omega$  is  $\Delta\Omega = \Delta\omega_i/\omega_{cli} \approx 0.006$ . Furthermore, the simulation results show that the vibration characteristics of inner and outer rotors are similar, so the analysis is focused on the dynamic response of disk 1 on the inner rotor.

Bifurcation diagrams, dynamic trajectories, Poincaré maps and spectrum graphs are employed to exhibit the results of numerical simulation. Dynamic trajectories represent the instantaneous positions of the rotor center. Spectrum graphs exhibit the frequency contents of the rotor response and are obtained from the Fourier transformation of the time series of rotor response in the vertical direction. Poincaré maps are determined by sampling the trajectory of the rotor center at a constant interval of the forcing period of  $T = 2\pi/\omega_i$  and projecting the outcome on the  $X(nT)$  versus  $Y(nT)$  plane. Bifurcation diagrams demonstrate the trajectory of the rotor in the vertical direction against the variation of speed parameter  $\Omega$ . In order to clearly demonstrate the variations of bifurcation with rotating speed, bifurcation diagrams are depicted with  $3\Delta\Omega$  as the speed interval in this research. To significantly improve the computational efficiency of generating bifurcation diagrams, a parallel computing strategy is adopted in MATLAB programming and is implemented at the workstation.

**Table 2.** The first three order critical speeds of MSDS.

Order	Inner Rotor Excitation (rad/s)		Outer Rotor Excitation (rad/s)	
	$r=1.2$	$r=-1.2$	$r=1.2$	$r=-1.2$
1	828.48	828.47	828.46	828.46
2	1025.9	1023.2	1010.7	1008.5
3	3293.2	3289.5	3287.2	3284.1

### 3.1. Nonlinear Dynamic Responses

In the case of  $r = 1.2$ , the types of bifurcation for the inner rotor response without rubbing are examined with the increase of speed parameter  $\Omega$ , and the corresponding bifurcation diagrams are generated in Figure 7. After careful inspection, each speed corresponds to five points, which indicates that the MSDS always performs the sub-synchronous vibration of period 5 over the full speed range. It should be noted that for some speed ranges, the number of points displayed is less than five due to multiple close response amplitude points at the speed shown in a larger scale figure, as shown in Figure 8a,c. In some intervals, the number of points for some rotational speeds is also less than five, while the corresponding Poincaré diagram shows that the number of points is still five. The reason is that displacements in the vertical direction that are intercepted by the bifurcation diagram at this moment are almost equal, as illustrated in Figure 8b. It should be noted that the dynamic trajectories in Figure 8, “○” and “△”, respectively, represent the positions of rotor center at a certain moment and the subsequent moment, according to which the change of the rotor whirling trajectory with time is demonstrated and the whirling direction of the rotor can be judged.

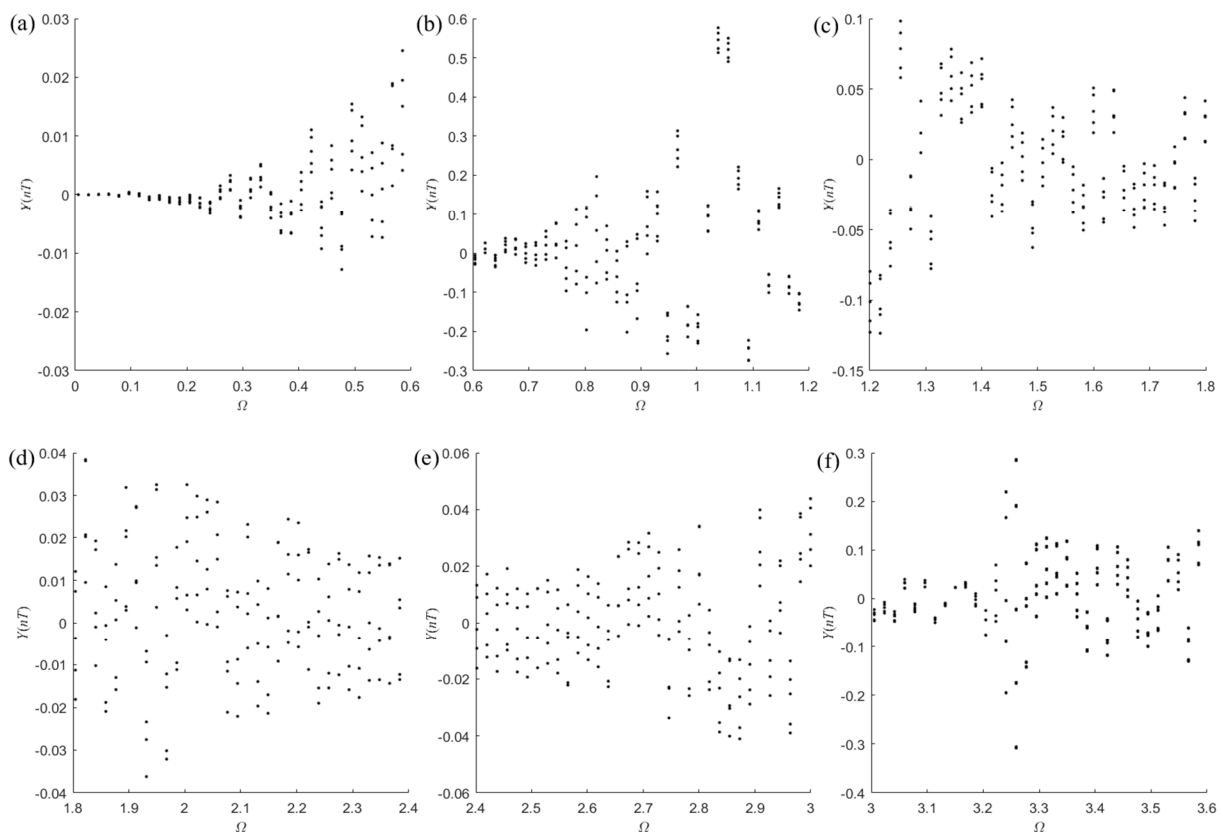


**Figure 7.** Bifurcation diagram of MSDS response without rubbing in co-rotation with  $r = 1.2$ . (a)  $0.006 \leq \Omega \leq 0.6$ , (b)  $0.6 \leq \Omega \leq 1.2$ , (c)  $1.2 \leq \Omega \leq 1.8$ , (d)  $1.8 \leq \Omega \leq 2.4$ , (e)  $2.4 \leq \Omega \leq 3.0$ , (f)  $3.0 \leq \Omega \leq 3.6$ .

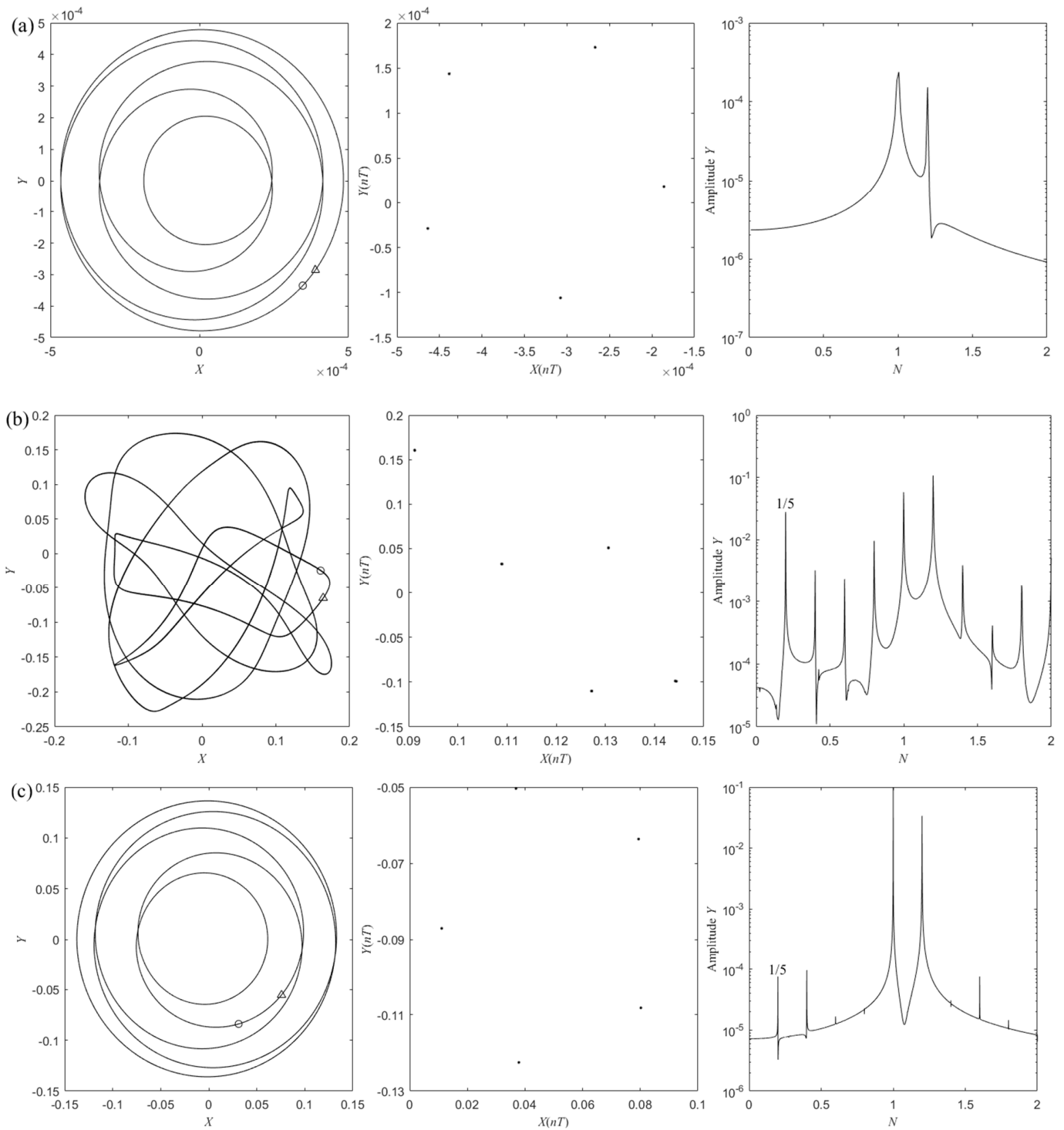


**Figure 8.** Trajectories, Poincaré maps and spectrograms of MSDS response in co-rotation with  $r = 1.2$ . (a) Period 5 motion with  $\Omega = 0.096$ , (b) Period 5 motion with  $\Omega = 1.090$ , (c) Period 5 motion with  $\Omega = 3.549$ .

In the case of  $r = 1.2$  without rubbing, the vibration of MSDS is mainly dominated by the dual-frequency unbalanced excitation of inner and outer rotors. More specifically, it is determined by the speed ratio and rotational frequency difference of inner and outer rotors. Taking Figure 8a as an example, there are two dimensionless frequency components of 1 and 1.2 in the spectrum, namely the dimensionless rotating frequencies of inner and outer rotors. In Figure 8b, the dimensionless rotating frequency difference 1/5 and its

multiple frequency components also appear in the spectrum. The most likely cause of this phenomenon is the operation of MSDS near the first-order critical speed. As a result, the MSDS is dominated by the sub-synchronous vibration of period 5 without rubbing when the speed ratio is  $r = 1.2$ .

In the case of  $r = 1.2$  with rubbing, the bifurcation diagrams are provided in Figure 9. For the range  $0 < \Omega \leq 0.978$ , the rotor response is the period 5 vibration. For  $\Omega = 0.984$  and  $0.990 \leq \Omega \leq 1.002$ , the responses of period 20 and period 15 are observed, respectively. With further increase of  $\Omega$ , the sub-synchronous vibration of period 5, quasi-periodic and chaotic vibration are observed alternately. Period 5 vibration occurs in the ranges  $\Omega = 1.008$ ,  $1.074 \leq \Omega \leq 1.110$  and  $1.123 \leq \Omega \leq 1.129$ . Quasi-periodic vibration is observed to exist in the ranges  $1.020 \leq \Omega \leq 1.038$ ,  $\Omega = 1.116$ ,  $1.153 \leq \Omega \leq 1.159$  and  $1.183 \leq \Omega \leq 1.195$ . Chaotic vibration is seen in the ranges  $\Omega = 1.014$ ,  $1.044 \leq \Omega \leq 1.068$ ,  $1.165 \leq \Omega \leq 1.177$  and  $1.201 \leq \Omega \leq 1.304$ . Period 5 vibration is largely seen to dominate the rotor response for the range  $1.310 \leq \Omega \leq 3.6$ , except at  $\Omega = 3.253$  where chaotic vibration is observed. By comparing Figures 7 and 9, it is found that rubbing will cause stable multiple periodic motion, critical quasi-periodic motion and unstable chaotic motion.

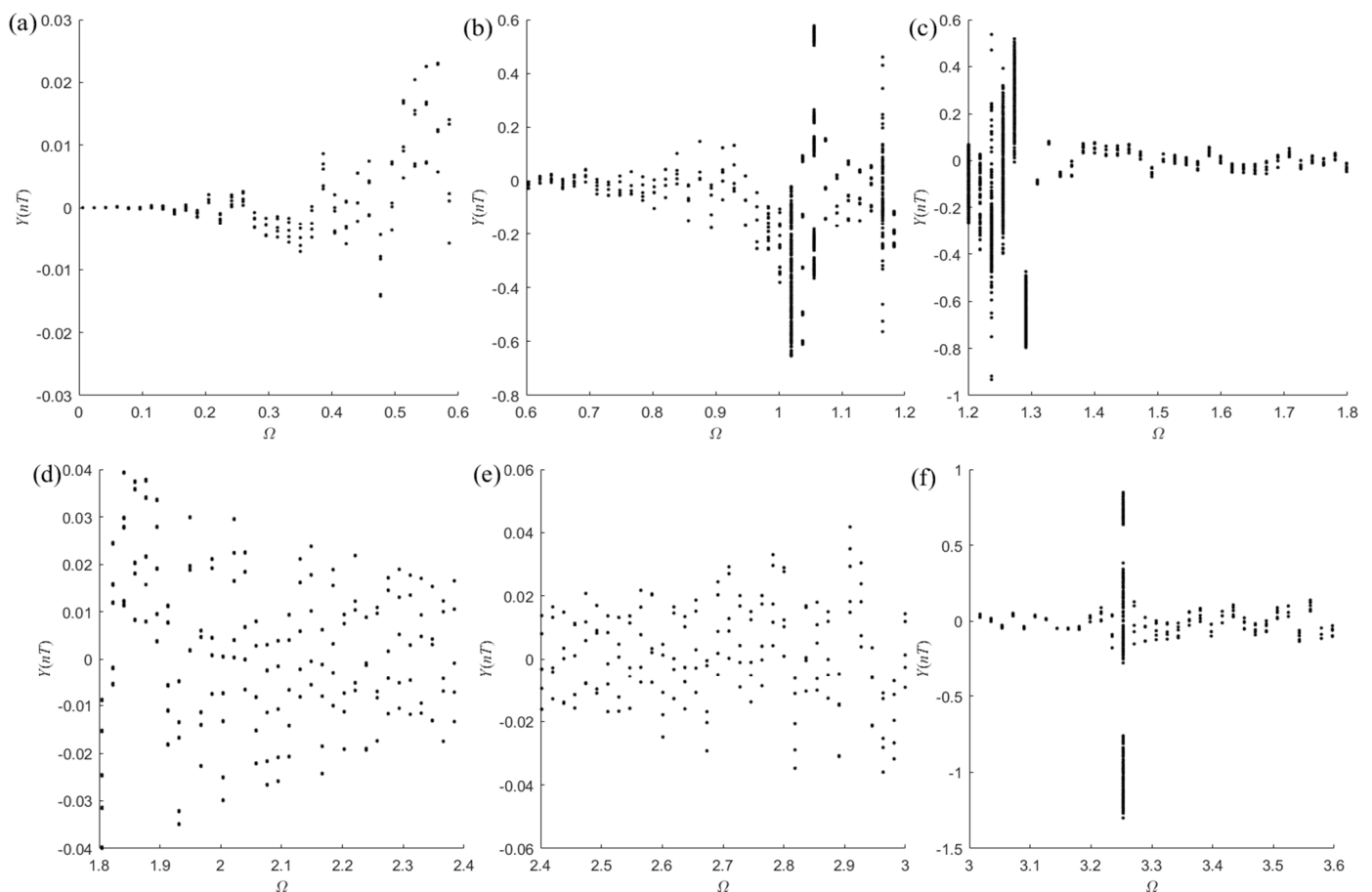


**Figure 9.** Bifurcation diagram of MSDS response with rubbing in co-rotation  $r = 1.2$ . (a)  $0.006 \leq \Omega \leq 0.6$ , (b)  $0.6 \leq \Omega \leq 1.2$ , (c)  $1.2 \leq \Omega \leq 1.8$ , (d)  $1.8 \leq \Omega \leq 2.4$ , (e)  $2.4 \leq \Omega \leq 3.0$ , (f)  $3.0 \leq \Omega \leq 3.6$ .

In order to have a deep insight into the above abundant nonlinear vibrations stimulated by rubbing, the dynamic responses of period 5, 15, 20, quasi-periodic and chaotic vibration at  $\Omega = 1.008$ ,  $\Omega = 0.996$ ,  $\Omega = 0.984$ ,  $\Omega = 1.032$  and  $\Omega = 1.044$  are depicted in Figure 10. It is easy to observe that the period  $n$  motion is characterized by  $n$  points in Poincaré maps, and the minimum dimensionless frequency component in the spectrum is  $1/n$ . In addition, the response trajectory becomes more complicated with larger  $n$ , as shown in Figure 10a–c. When ghosting appears in the trajectory in Figure 10d, the Poincaré map is exhibited as

five closed elliptic curves, and the frequency components with clear contours can still be observed in the spectrum, which infers that MSDS performs a quasi-periodic motion. Furthermore, chaotic motion occurs when the trajectory becomes chaotic, many irregular points exist in the Poincaré diagram, and dense burrs appear in the spectrum, as depicted in Figure 10e.

In the above nonlinear dynamic behaviors in co-rotation with  $r = 1.2$ , the high-order sub-synchronous motion of period 15 and period 20 are multiples of five, corresponding to the rotating frequency difference  $1/5$  with speed ratio  $r = 1.2$ . Under the combined actions of exponential order rubbing force, nonlinear electromagnetic force and unbalanced force, the fractional frequency components  $1/15$  and  $1/20$  are excited, which corresponds to  $1/3$  and  $1/4$  of the rotational frequency difference  $1/5$ , respectively. Accordingly, in the spectrums in Figure 10b,c, the frequency components can be regularly expressed as multiple frequency components of  $1/15$  and  $1/20$ , respectively. Even for the quasi-periodic and chaotic motions, the main frequency components in the spectrums can be expressed as a series of combined frequency components of the rotating frequency difference  $1/5$  and its fractional frequency component  $1/25$ , as shown in Figure 10d,e. Therefore, the nonlinear vibration characteristics of MSDS are closely related to the speed ratio.

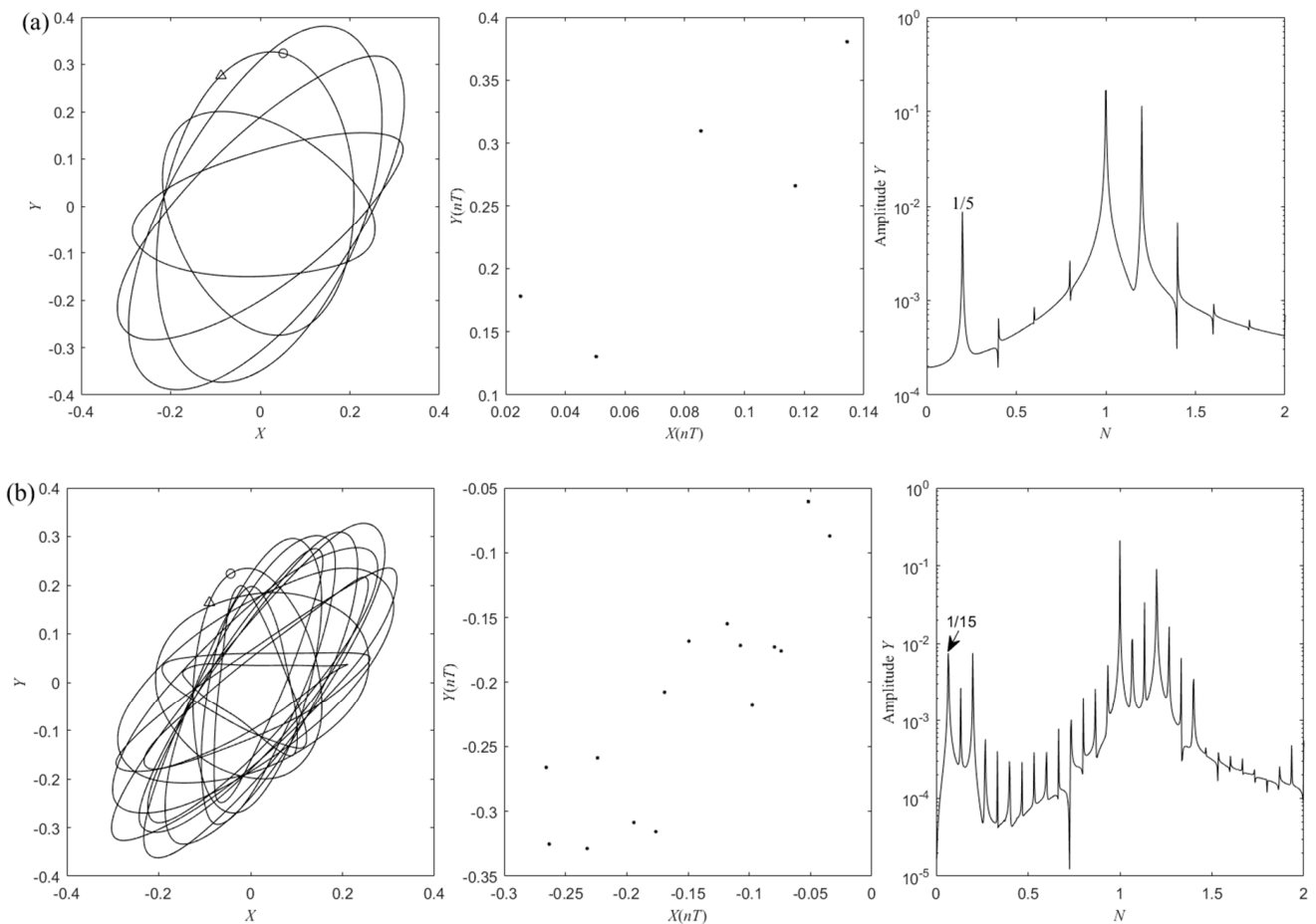
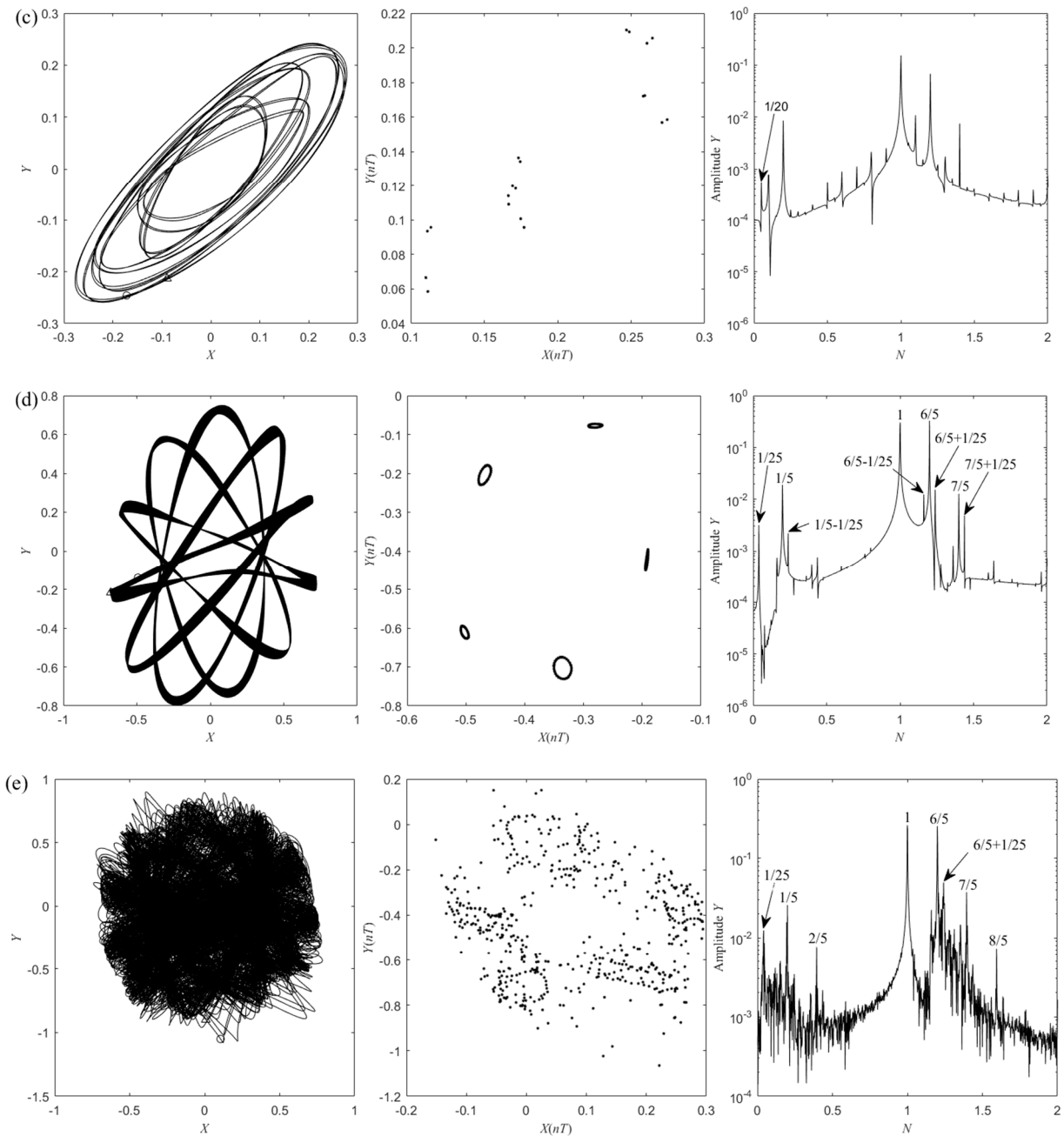


Figure 10. Cont.



**Figure 10.** Trajectories, Poincaré maps and spectrograms of MSDS response in co-rotation with  $r = 1.2$ . (a) Period 5 motion with  $\Omega = 1.008$ , (b) Period 15 motion with  $\Omega = 0.996$ , (c) Period 20 motion with  $\Omega = 0.984$ , (d) Quasi-periodic motion with  $\Omega = 1.032$ , and (e) Chaotic vibration with  $\Omega = 1.044$ .

With parameters unchanged in counter-rotation  $r = -1.2$ , the bifurcation diagrams of MSDS are shown in Figure 11. For  $0 < \Omega \leq 0.972$ , the rotor response is period 5. The attractors of period 10, 20, and 15 are, respectively, observed for  $\Omega = 0.978$ ,  $\Omega = 0.984$  and  $\Omega = 0.996$ , and the rotor response is chaos at  $\Omega = 0.990$ . With further increase of  $\Omega$ , the alternation of chaotic vibration and sub-synchronous vibration of period 5 is captured, except for  $\Omega = 1.044$  and  $1.889$  where period 10 vibration is observed, for  $\Omega = 1.919$  where period 15 vibration is seen, and for  $\Omega = 1.183$  where the response is quasi-periodic. Chaotic vibration is seen to exist in the ranges  $1.002 \leq \Omega \leq 1.038$ ,  $1.159 \leq \Omega \leq 1.177$ ,  $1.225 \leq \Omega \leq 1.267$ ,  $1.316 \leq \Omega \leq 1.340$ ,  $\Omega = 1.786$  and  $1.805 \leq \Omega \leq 1.835$ . The existence of period 5 vibration is found in the ranges  $1.050 \leq \Omega \leq 1.153$ ,  $1.189 \leq \Omega \leq 1.219$ ,  $1.273 \leq \Omega \leq 1.310$ ,  $1.346 \leq \Omega \leq 1.780$ ,  $1.792 \leq \Omega \leq 1.799$  and  $1.841 \leq \Omega \leq 1.925$ . Quasi-periodic vibration is found in the

ranges  $1.931 \leq \Omega \leq 1.961$  and  $2.022 \leq \Omega \leq 2.046$ . For the ranges  $1.968 \leq \Omega \leq 1.980$ ,  $2.004 \leq \Omega \leq 2.016$  and specific speed  $\Omega = 1.986$ , period 5, 20 and 10 vibrations are observed. The response is chaotic in the ranges  $1.992 \leq \Omega \leq 1.998$  and  $2.052 \leq \Omega \leq 2.094$ . Period 5 vibration dominates the response for the range  $2.100 \leq \Omega \leq 3.6$ , except for chaos vibration in the small range  $3.313 \leq \Omega \leq 3.319$ .

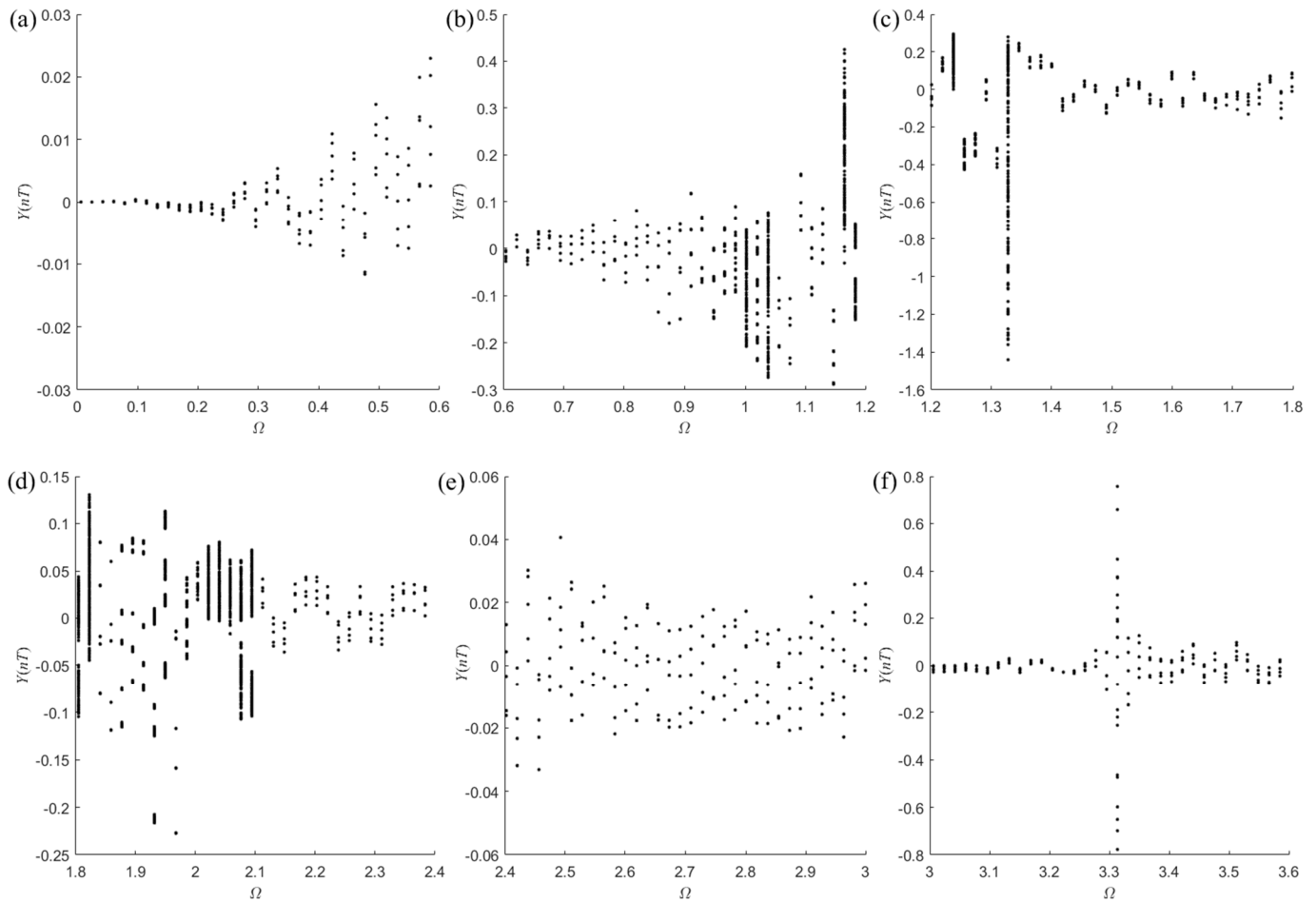


**Figure 11.** Bifurcation diagram of MSDS response with rubbing in counter-rotation  $r = -1.2$ . (a)  $0.006 \leq \Omega \leq 0.6$ , (b)  $0.6 \leq \Omega \leq 1.2$ , (c)  $1.2 \leq \Omega \leq 1.8$ , (d)  $1.8 \leq \Omega \leq 2.4$ , (e)  $2.4 \leq \Omega \leq 3.0$ , (f)  $3.0 \leq \Omega \leq 3.6$ .

As typical examples of nonlinear dynamic behaviors in counter-rotation with  $r = -1.2$ , the sub-synchronous vibrations of period 10, 15, 20, quasi-periodic and chaotic vibration are illustrated in Figure 12 at  $\Omega = 0.978$ ,  $\Omega = 0.996$ ,  $\Omega = 0.984$ ,  $\Omega = 1.183$  and  $\Omega = 2.052$ , respectively. In the case of rubbing, the dynamic response characteristics for counter-rotation with  $r = -1.2$  are almost the same as those of co-rotation with  $r = 1.2$ . When MSDS performs sub-synchronous vibrations of period  $n$  with  $n = 10, 15$  and  $20$ , its frequency components can be expressed as multiple times of the fractional frequency  $1/n$  corresponding to the rotating frequency difference  $1/5$ . For the quasi-periodic motion and chaotic motion, the main frequency components can be expressed as various combined frequency components of rotating frequency difference  $1/5$  and its fractional frequency. Therefore, the nonlinear dynamic characteristics for counter-rotation with rubbing are also determined by the speed ratio. In addition, it can be observed that the rotor alternately performs forward whirl and backward whirl in the dynamic trajectories in Figure 12a–d, while the rotor only performs forward whirl in the dynamic trajectories in Figure 10a–d. It implies that the dynamic response of MSDS in counter-rotation is more complicated than that in co-rotation.

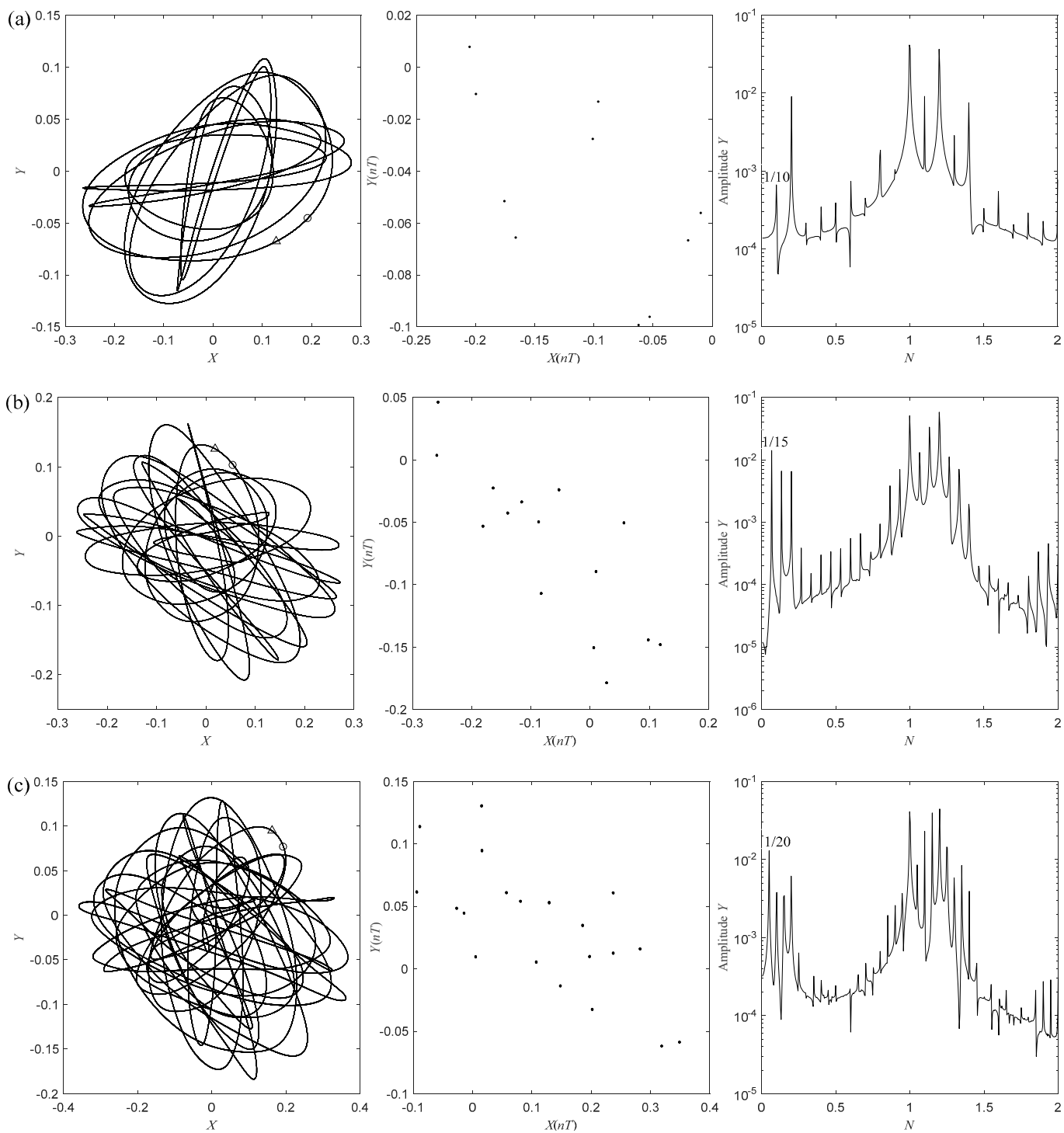
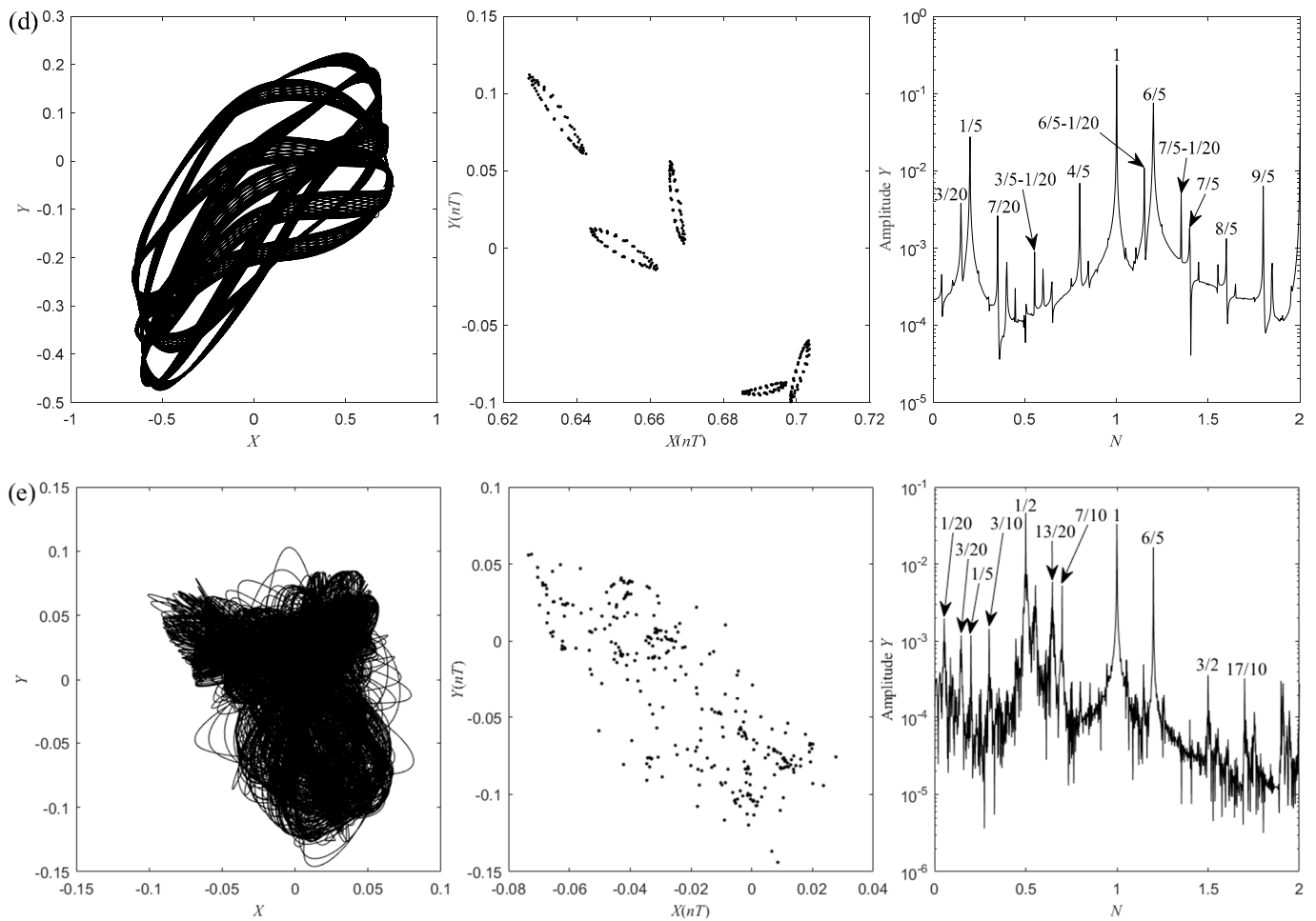


Figure 12. Cont.



**Figure 12.** Trajectories, Poincaré maps and spectrograms of MSDS response in counter-rotation with  $r = -1.2$ . (a) Period 10 motion with  $\Omega = 0.978$ , (b) Period 15 motion with  $\Omega = 0.996$ , (c) Period 20 motion with  $\Omega = 0.984$ , (d) Quasi-periodic motion with  $\Omega = 1.183$ , (e) Chaotic vibration with  $\Omega = 2.052$ .

From the above analysis, it is obvious that the sub-synchronous vibration of period 5 is the fundamental motion under fixed-point rubbing with  $r = \pm 1.2$ . In contrast to co-rotation  $r = 1.2$ , the dynamic responses in counter-rotation  $r = -1.2$  are more complicated due to the opposite direction of the gyroscopic moment. More specifically, period  $n$  ( $n = 5m$ ,  $m = 2, 3, 4, \dots$ ), quasi-periodic and chaotic vibrations span wider speed ranges and occur more frequently in counter-rotation, which is also tenable for other speed ratios.

### 3.2. Influence of Speed Ratio

To investigate the effects of speed ratio on the bifurcation characteristics of MSDS, the bifurcation diagrams and nonlinear dynamic responses for  $r = 1.3$ ,  $r = 1.5$  and  $r = 2.0$  in co-rotation are investigated in this section.

When the speed ratio is  $r = 1.3$ , the bifurcation diagrams of MSDS are illustrated in Figure 13. By careful examination, sub-synchronous motion of period 10 is found to be the fundamental motion that dominates the dynamic responses.  $n = 10$  seems to correspond to the denominator of the rotational frequency difference  $3/10$ . In addition, sub-synchronous motion of period 20, quasi-periodic and chaotic motion mainly occur in the ranges  $1.104 \leq \Omega \leq 1.593$  and  $\Omega = 3.006$ . The dynamic responses of various typical motions are shown in Figure 14. Similarly, for the sub-synchronous motion of period 10 and period 20 in Figure 14a,b, the basic frequency components are  $1/10$  and  $1/20$ , respectively, and the other frequency components can be expressed as their multiple frequency components. In

quasi-periodic motion with at 10 closed curves in Figure 14c, the main frequency component can be expressed as the multiples of basic frequency component 1/10.

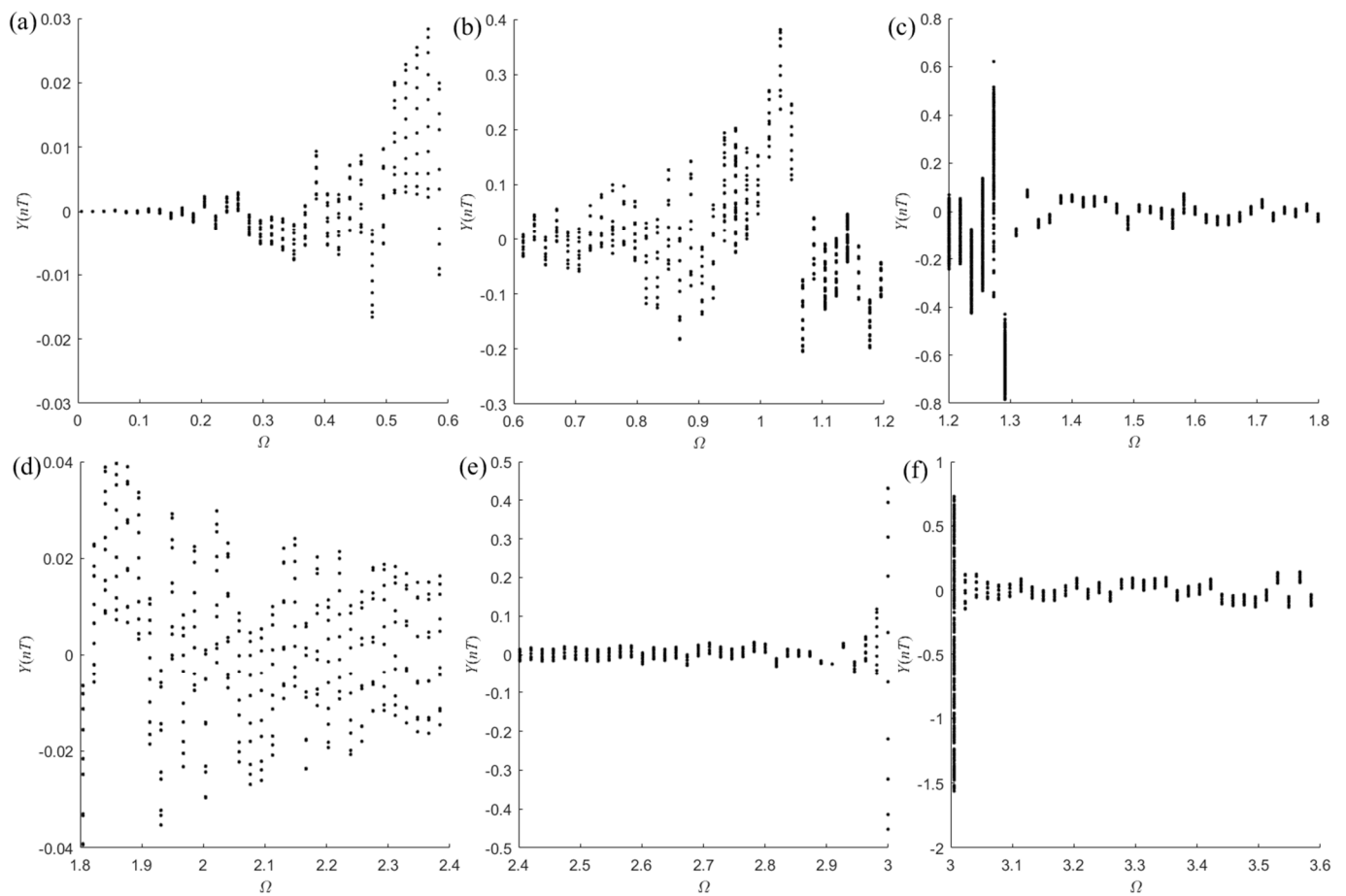


**Figure 13.** Bifurcation diagram of MSDS response with rubbing in co-rotation with  $r = 1.3$ . (a)  $0.006 \leq \Omega \leq 0.6$ , (b)  $0.6 \leq \Omega \leq 1.2$ , (c)  $1.2 \leq \Omega \leq 1.8$ , (d)  $1.8 \leq \Omega \leq 2.4$ , (e)  $2.4 \leq \Omega \leq 3.0$ , (f)  $3.0 \leq \Omega \leq 3.6$ .

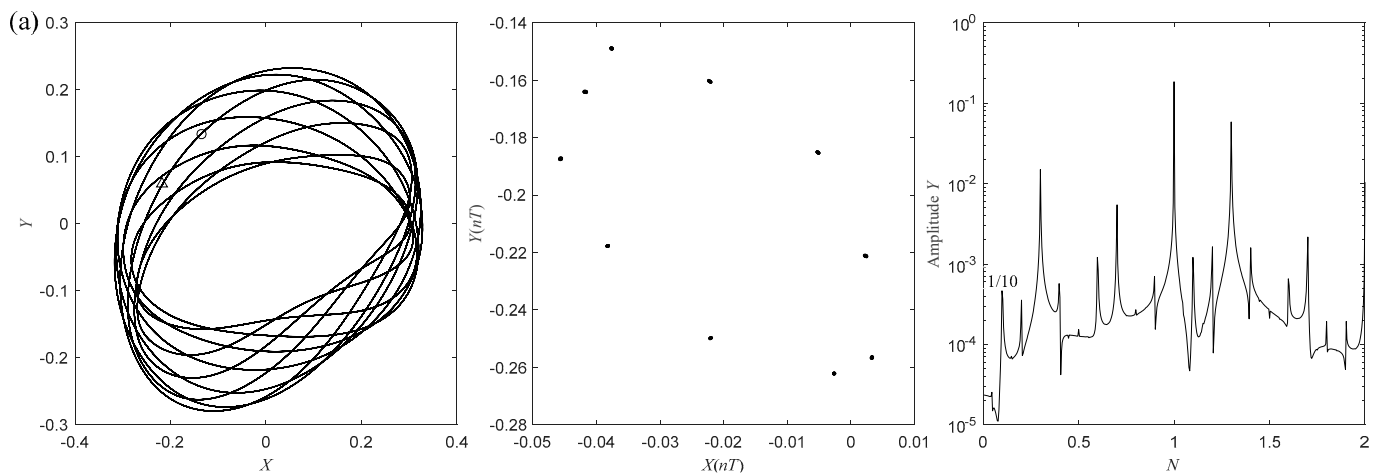


**Figure 14.** Cont.

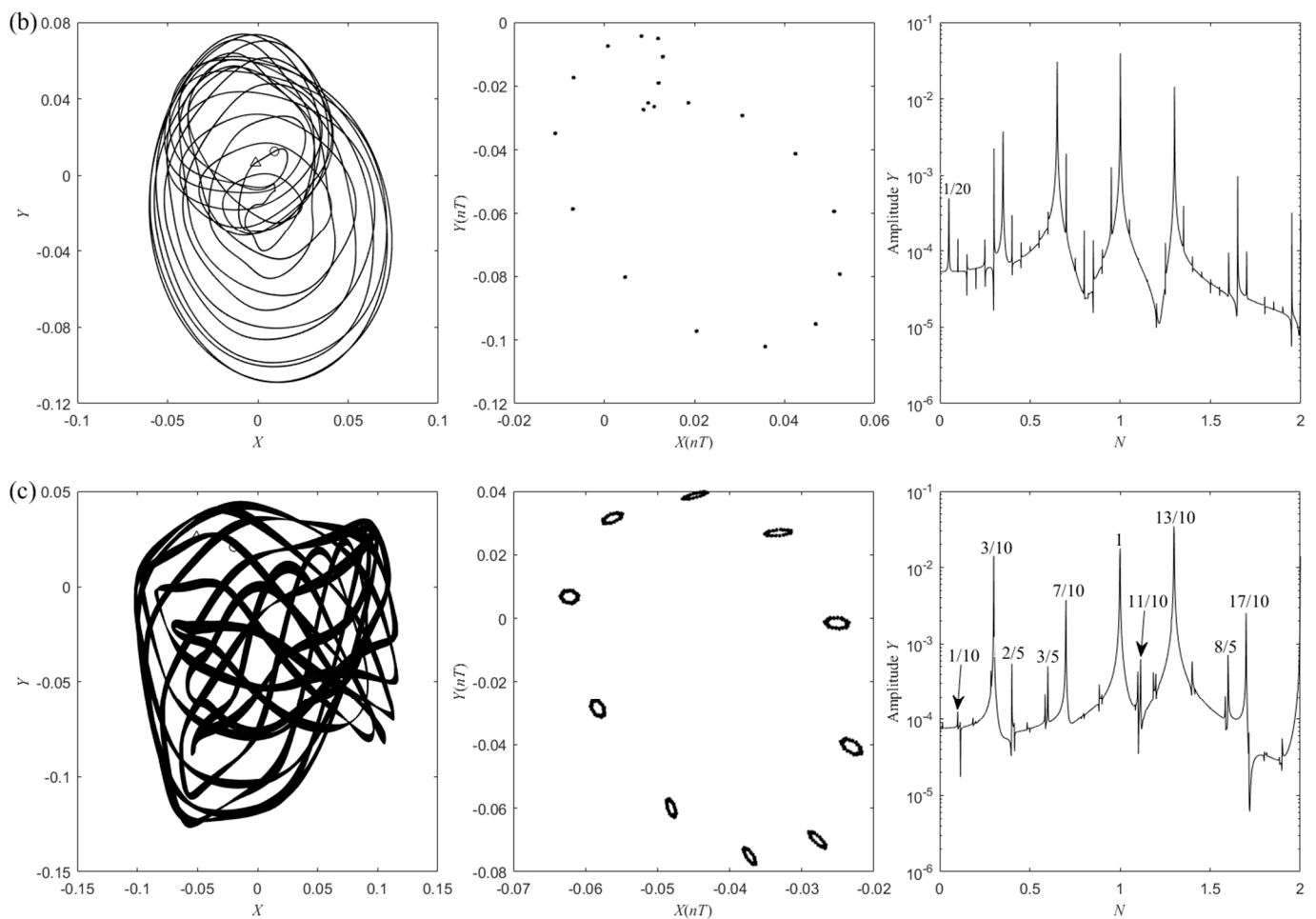


**Figure 14.** Trajectories, Poincaré maps and spectrograms of MSDS response in co-rotation with  $r = 1.3$ . (a) Period 10 motion with  $\Omega = 1.056$ , (b) Period 20 motion with  $\Omega = 1.587$ , (c) Quasi-periodic motion with  $\Omega = 1.104$ .

The bifurcation diagrams and corresponding typical dynamic responses of MSDS with speed ratio  $r = 1.5$  are provided in Figures 15 and 16, respectively. In this situation, the period 2 vibration dominates the whole speed range, where  $n = 2$  is equal to the denominator of the rotational frequency difference  $\frac{1}{2}$ . Quasi-periodic motion and chaotic motion exist in the ranges  $1.129 \leq \Omega \leq 1.255$  and  $2.384 \leq \Omega \leq 2.619$ . A double period 4 motion at  $\Omega = 0.845$ , multiple period 28 vibration at  $\Omega = 1.213$  and the quasi-period motion with two closed curves at  $\Omega = 1.044$  are demonstrated as typical examples of dynamic responses in Figure 16. The sub-synchronous motion of period  $n$  is characterized by  $n$  points in the Poincaré maps and the basic frequency component  $1/n$ . The main frequency components of quasi-period motion may be expressed as the combination of rotational frequency difference  $1/2$  and its fractional frequency  $1/10$ , for example,  $1/5 = 2 \times 1/10$ ,  $3/10 = 1/2 - 2 \times 1/10$ , and so on.

The bifurcation diagrams and corresponding typical dynamic responses of MSDS with speed ratio  $r = 2$  are depicted in Figures 17 and 18. It is obvious that the simplest form of motion, sub-synchronous motion of period 1, namely synchronous motion, occupies an absolute advantage over other forms of motion. Also, the 1 in period 1 corresponds to the rotating frequency difference 1 in the case of  $r = 2$ . The sub-synchronous motion of period 2, quasi-periodic motion and chaotic motion mainly appear in the range of  $1.165 \leq \Omega \leq 1.219$ ,  $1.986 \leq \Omega \leq 2.456$ ,  $2.837 \leq \Omega \leq 2.861$ , respectively, and their spectral characteristics are similar to those of other speed ratios.

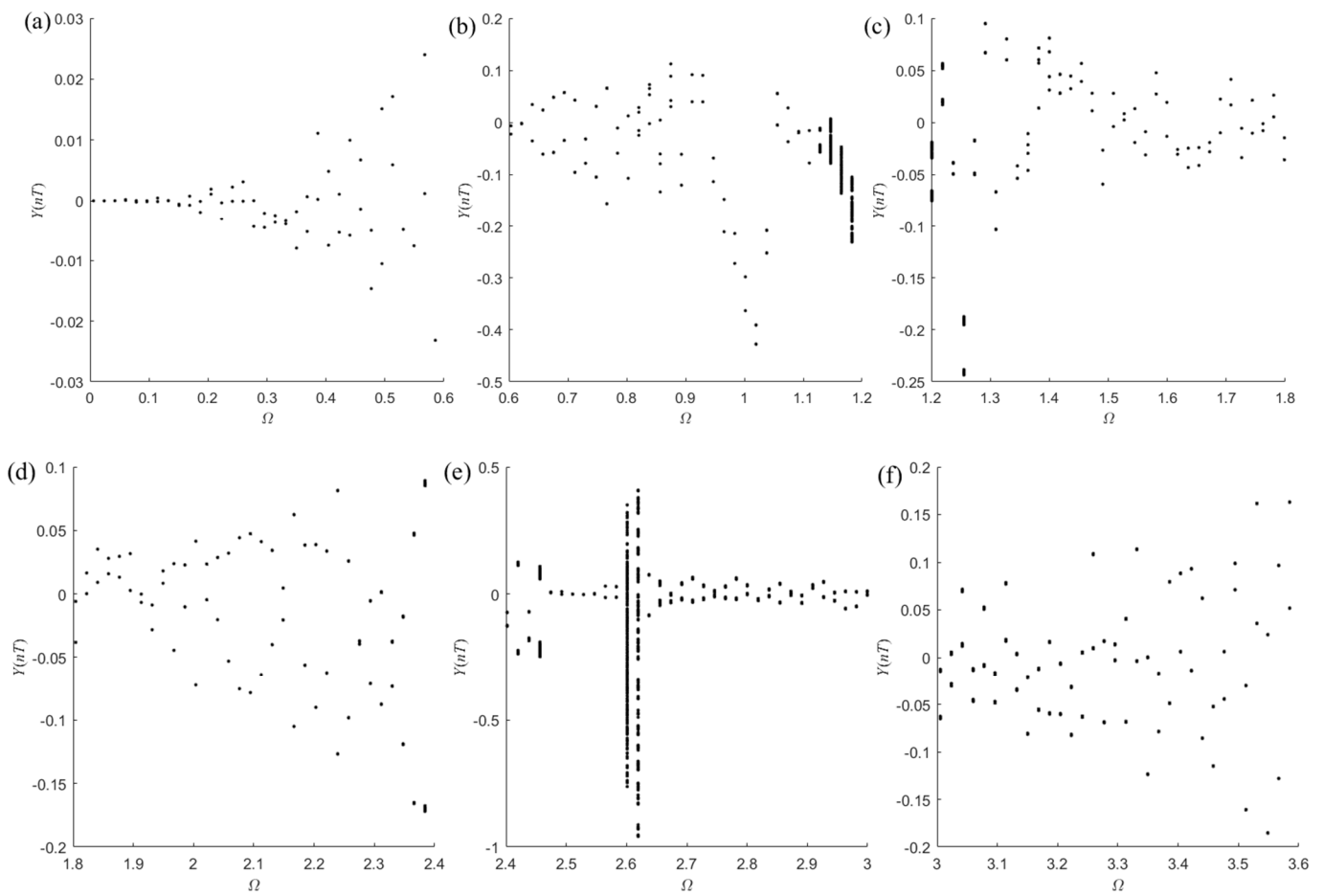


**Figure 15.** Bifurcation diagram of MSDS response with rubbing in co-rotation with  $r = 1.5$ . (a)  $0.006 \leq \Omega \leq 0.6$ , (b)  $0.6 \leq \Omega \leq 1.2$ , (c)  $1.2 \leq \Omega \leq 1.8$ , (d)  $1.8 \leq \Omega \leq 2.4$ , (e)  $2.4 \leq \Omega \leq 3.0$ , (f)  $3.0 \leq \Omega \leq 3.6$ .

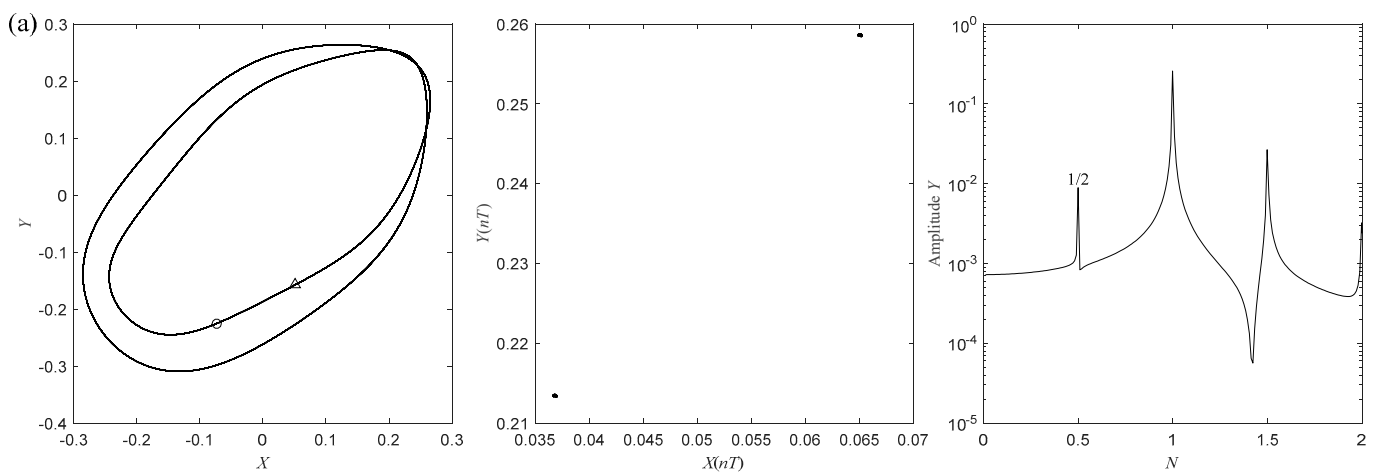


**Figure 16.** Cont.

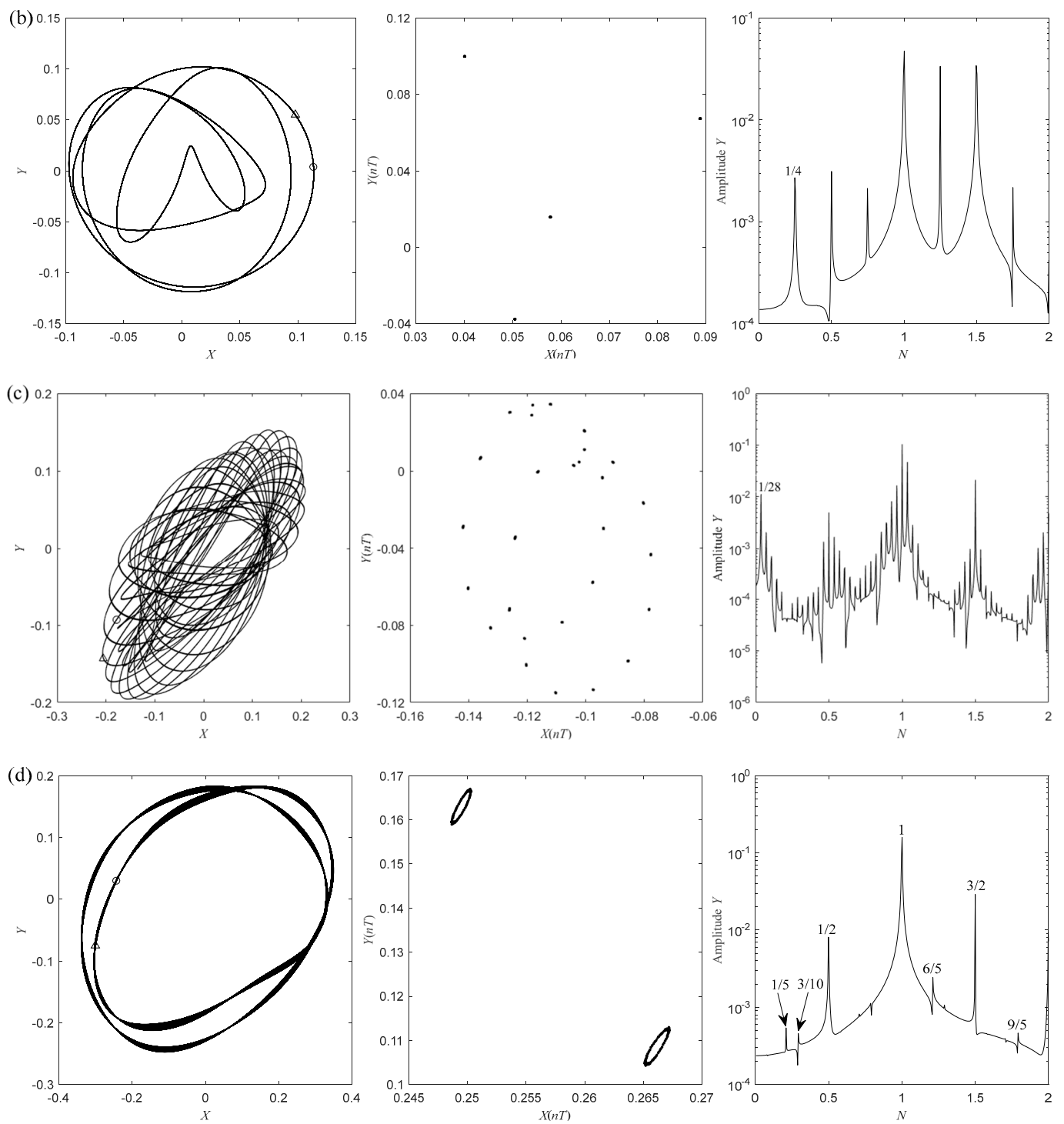


**Figure 16.** Trajectories, Poincaré maps and spectrograms of MSDS response in co-rotation with  $r = 1.5$ . (a) Period 2 motion with  $\Omega = 0.990$ , (b) Period 4 motion with  $\Omega = 0.845$ , (c) Period 28 motion with  $\Omega = 1.213$ , (d) Quasi-periodic motion with  $\Omega = 1.044$ .

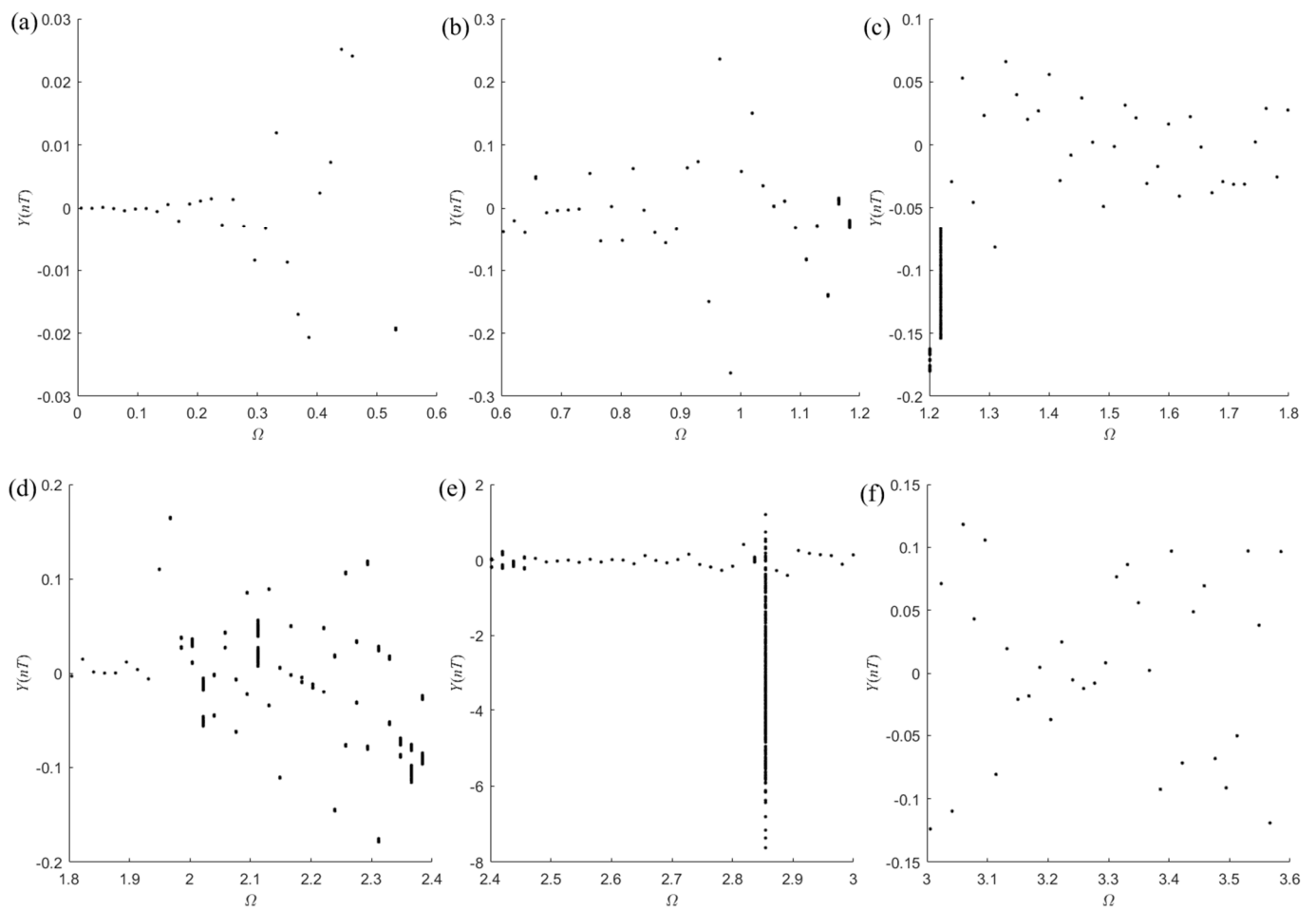


**Figure 17.** Bifurcation diagram of MSDS response with rubbing in co-rotation with  $r = 2$ . (a)  $0.006 \leq \Omega \leq 0.6$ , (b)  $0.6 \leq \Omega \leq 1.2$ , (c)  $1.2 \leq \Omega \leq 1.8$ , (d)  $1.8 \leq \Omega \leq 2.4$ , (e)  $2.4 \leq \Omega \leq 3.0$ , (f)  $3.0 \leq \Omega \leq 3.6$ .

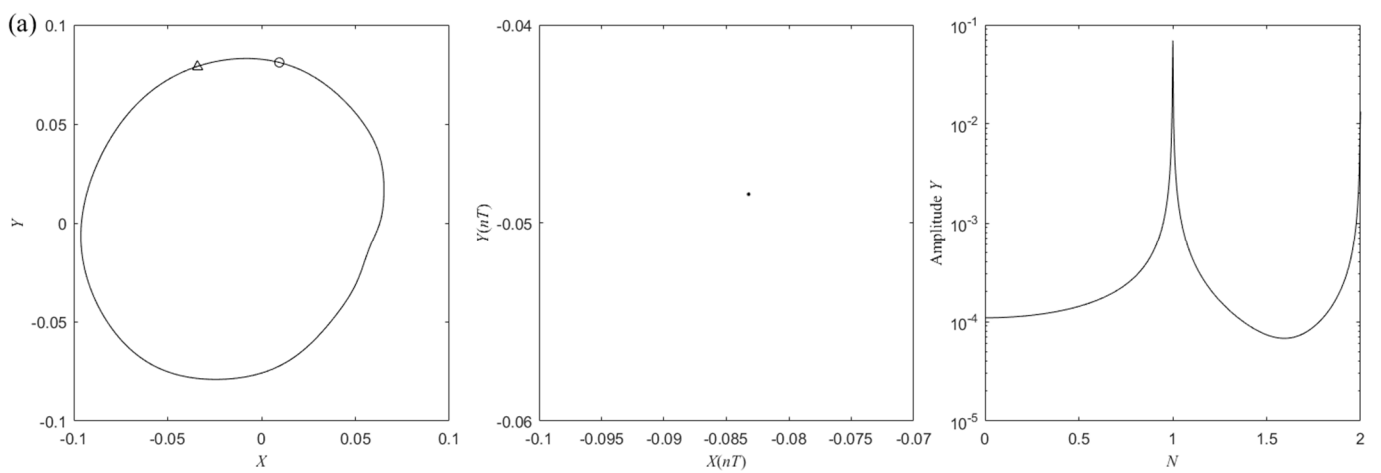


**Figure 18.** Cont.

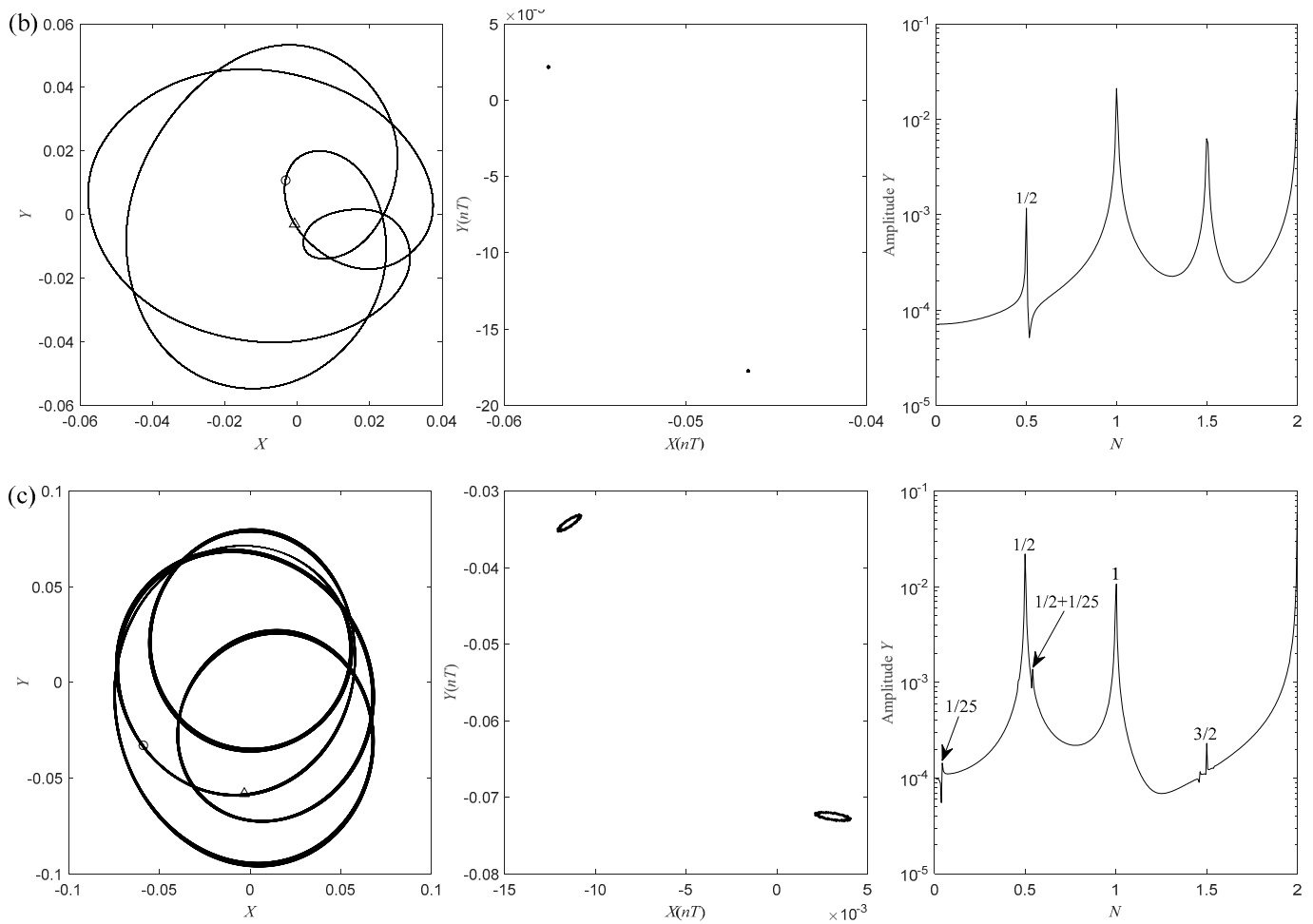


**Figure 18.** Trajectories, Poincaré maps and spectrograms of MSDS response in co-rotation with  $r = 2.0$ . (a) Synchronous motion with  $\Omega = 0.845$ , (b) Period 2 motion with  $\Omega = 0.664$ , (c) Quasi-periodic motion with  $\Omega = 1.998$ .

It is shown from the above analysis that the nonlinear vibration characteristics of MSDS with fixed-point rubbing mainly depend on the speed ratio. First, the most basic sub-synchronous vibration of period  $n$  is determined by the speed ratio  $r$ . The relationship between  $n$  and  $r$  is that  $n$  equals the greatest common divisor (GCD) of 10 times 1 and  $r$  divided by 10, i.e.,  $n = 10/\text{GCD}(10 \times [1 \cdot r])$ , which is listed in Table 3. The minimum dimensionless frequency component is  $1/n$  for the basic motion in the spectrum and other frequency components can be expressed as integer multiples of  $1/n$ . These two laws are also applicable to the higher order sub-synchronous motion of period  $mn$  ( $m = 2, 3, 4, \dots$ ). Second, quasi-periodic motion with speed ratio  $r$  is characterized by  $mn$  closed curves, and its main frequency components can be expressed as a variety of the combined frequency components of rotating frequency difference  $r-1$  and its fractional frequency, which is also suitable for chaotic motion with the same speed ratio. It should be pointed out that the above characteristics are also verified by the bifurcation diagrams of other speed ratios, which are neglected for simplicity. Consequently, it clearly states that speed ratio has considerable influence on the nonlinear dynamic characteristics of MSDS. Actually, the influence of speed ratio is achieved by the coupling effects of inter-shaft bearings and plentiful nonlinear dynamic behaviors reflect the strong cross-excitation phenomenon between inner and outer rotors, which is one of the most significant differences between dual-rotor systems and single-rotor systems.

**Table 3.** The relationship between  $n$  and speed ratio  $r$ .

$n$	1		2	5				10			
Speed ratio $r$	1	2	1.5	1.2	1.4	1.6	1.8	1.1	1.3	1.7	1.9

Another interesting phenomenon is the speed ranges where complicated dynamic responses exist. Except for the most basic motion for each speed ratio, high-order sub-synchronous motions, quasi-periodic and chaotic motions are generally excited near the critical speeds of MSDS. Taking  $r = 1.2$  in co-rotation in Figure 9 for an example, the sub-synchronous vibrations, except for period 5, mainly exist in the range  $0.984 \leq \Omega \leq 1.304$ , which includes the first two order critical speeds excited by the inner rotor, namely  $\Omega_{c1i} = 1$  and  $\Omega_{c2i} = 1.238$ . For the chaotic vibration at  $\Omega = 3.253$ , it is close to the inner rotor speed  $\Omega_{3i} = \Omega_{c3o}/r = 3.306$ , corresponding to the third order critical speed  $\Omega_{c3o} = 3.968$  excited by the outer rotor. It indicates that the motions near critical speeds are much more complicated than those away from them. The main reason is due to the fact that the vibration amplitude is larger and the rubbing response is more intense when the MSDS operates near the critical speeds, so the friction force during the rub impact process increases. Since the direction of the friction force is always opposite to the rotation direction of rotors, it will drive the rotor to whirl backward when its amplitude increases to a certain value, thus resulting in more complicated nonlinear vibrations.

### 3.3. Parameter Selection

During the operation of rotating machinery, prolonged exposure to fluctuating stresses caused by non-synchronous vibrations may result in the fatigue failure of rotor components [20–22]. In general, the alternating frequency of fluctuating stress increases with the complexity of asynchronous motion, and high alternating frequency will accelerate fatigue failure. Therefore, non-synchronous vibrations, especially high-order sub-synchronous motion, quasi-periodic motion and chaotic motion, are undesirable.

It is found from the above analysis that the rotor motion is synchronous only when the speed ratio is an integer. However, the speed ratio is usually not an integer, so the MSDS will inevitably undergo non-synchronous motion even without rubbing. From the perspective of reducing the severity of fluctuating stress, the complexity of nonlinear dynamic response should be reduced if possible. In other words, the speed ratio corresponding to smaller  $n$  is recommended to be selected.

Another more effective method is to take full advantage of the adjustable and controllable support characteristics of MSDS. With the real time adjustment of the support characteristics by the control system, the equivalent damping of AMBs can be increased to attenuate response amplitudes, and the equivalent stiffness can be changed to keep critical speeds away from the operating speeds of MSDS [13–15], which will bring the MSDS into fundamental sub-synchronous vibrations. For example, with a larger derivative coefficient of  $K_d = 0.0005$  and other parameters remaining the same, the bifurcation diagrams of rotor response for  $r = 1.2$  is depicted in Figure 19. Comparing Figures 9 and 19, it is obvious that except for the basic sub-synchronous vibration of period 5, other types of sub-synchronous vibrations disappear for larger  $K_d = 0.0005$ , especially for the range  $0.984 \leq \Omega \leq 1.304$ . It is exactly where the MSDS is superior to the traditional dual-rotor system. Nevertheless, the chaos vibration at  $\Omega = 3.254$ , corresponding to the first order bending modes, still exists for the reason that the derivative coefficient has little influence on this mode of the system [13], which deserves further investigation.

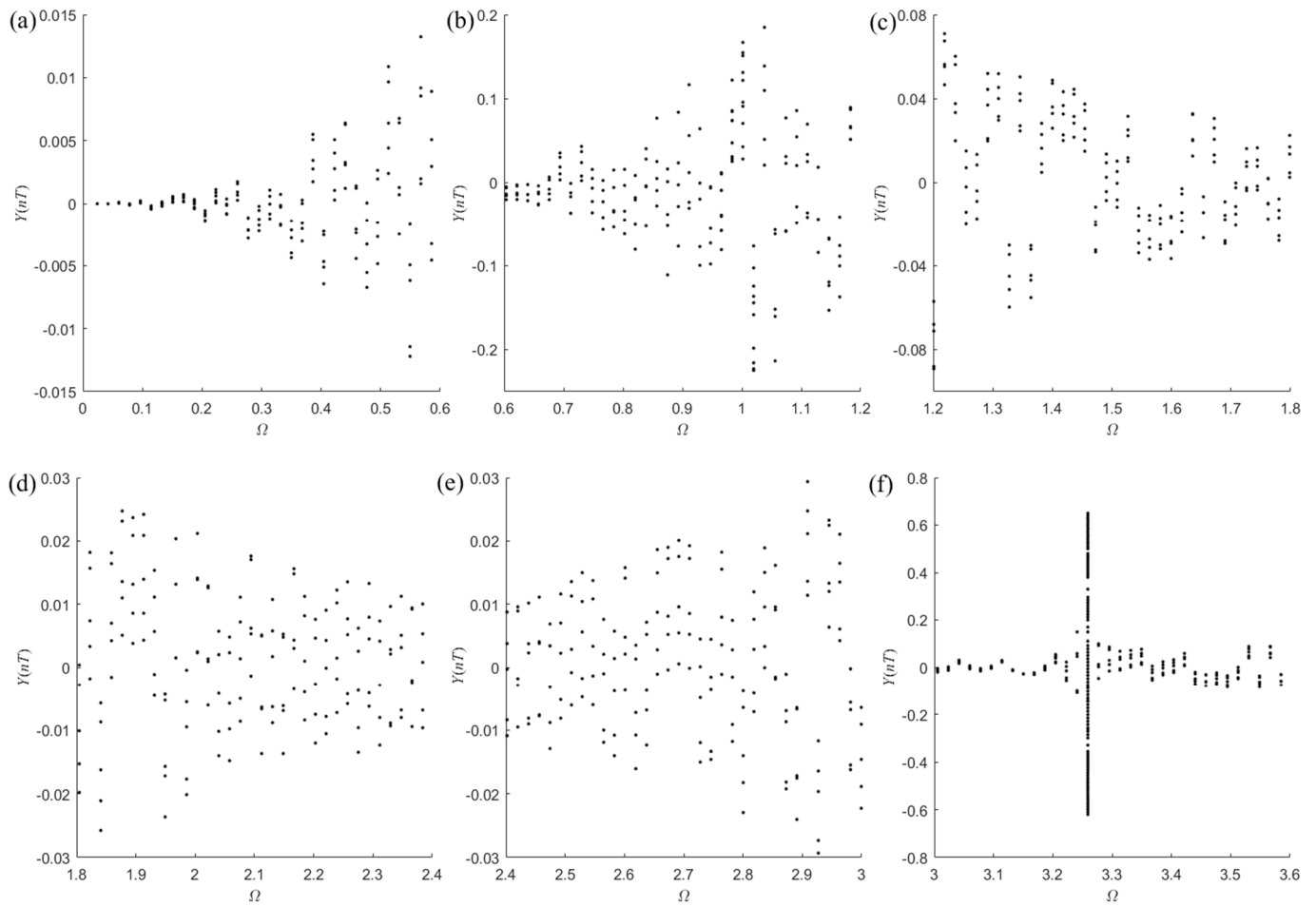


**Figure 19.** Bifurcation diagram of MSDS response with rubbing in co-rotation with  $r = 1.2$  and  $K_d = 0.0005$ . (a)  $0.006 \leq \Omega \leq 0.6$ , (b)  $0.6 \leq \Omega \leq 1.2$ , (c)  $1.2 \leq \Omega \leq 1.8$ , (d)  $1.8 \leq \Omega \leq 2.4$ , (e)  $2.4 \leq \Omega \leq 3.0$ , (f)  $3.0 \leq \Omega \leq 3.6$ .

In order to have an insight into the influence of AMB control parameters on MSDS nonlinear dynamics, the bifurcation diagrams of rotor response with proportional coefficient  $K_p$  and derivative coefficient  $K_d$  are shown in Figure 20, where  $\omega_i = 700 \text{ rad/s}$ ,  $r = 1.2$ , and other parameters remained the same with Table 1. In Figure 20a, MSDS performs the simplest sub-synchronous motion of period 5 when  $K_p$  is in the range  $1.8 \leq K_p \leq 39.4$  and it alternately performs high-order sub-synchronous motion, quasi-periodic motion and chaotic motion when  $K_p$  is beyond the range  $1.8 \leq K_p \leq 39.4$ . The reason is that increasing  $K_p$  will increase the equivalent stiffness of AMB, and too large or too small equivalent stiffness will make the operating speed close to a certain order critical speed of MSDS. In Figure 20b, MSDS performs the simplest sub-synchronous motion of period 5 when  $K_p$  is in the range  $0.0002 \leq K_d \leq 0.00086$ , and it performs complicated non-synchronous motions when  $K_d$  is small or large. The reason is that the AMB equivalent damping increases with  $K_d$ ; when equivalent damping is too small, the capacity of MSDS to attenuate vibration reduces, and when it is too large, it directly amplifies the influence of noise in differential signal on the system stability, resulting in unstable motions [23]. Therefore, it is necessary to select appropriate control parameters to make the MSDS perform the simplest sub-synchronous motion.

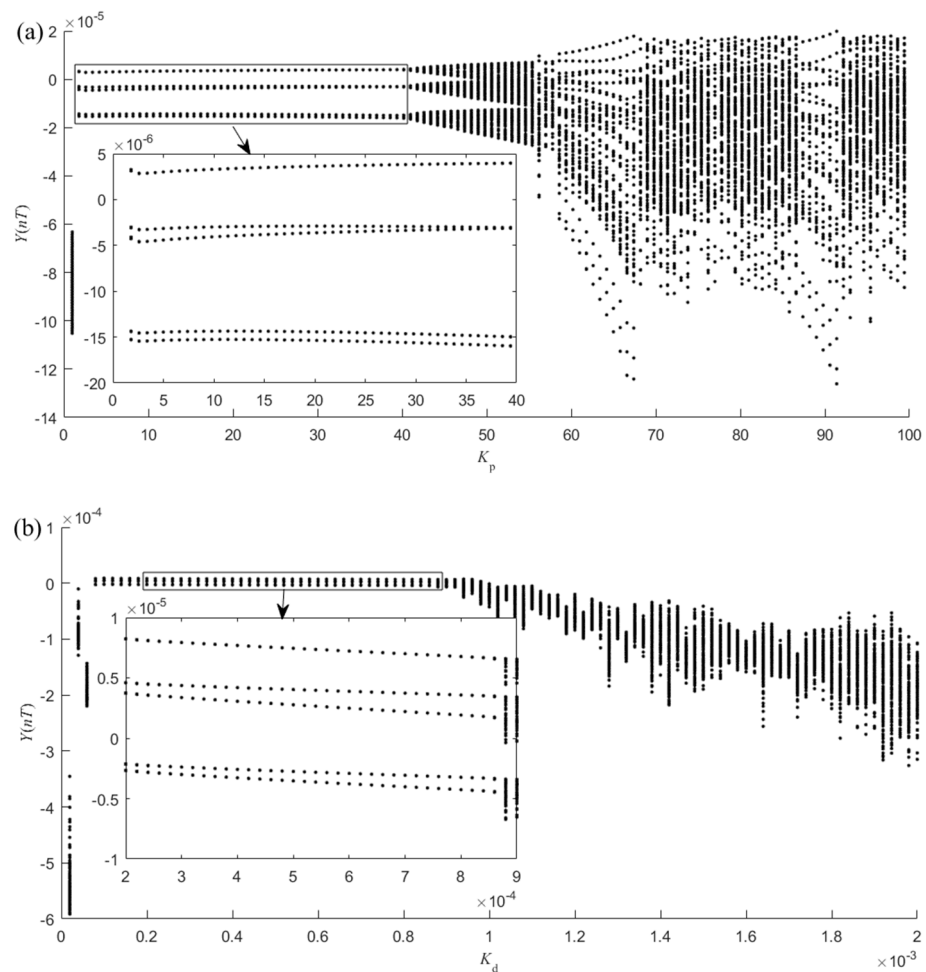


**Figure 20.** Bifurcation diagram of MSDS response with rubbing in co-rotation with  $r = 1.2$  and  $\omega_1 = 700$  rad/s. (a) Proportional coefficient  $K_p$ , (b) Derivative coefficient  $K_d$ .

In summary, there are three suggestions for parameter selection to keep the asynchronous vibrations of MSDS as simple as possible. First, the speed ratio  $r$  corresponding to smaller  $n$  is recommended, where  $n = 10/\text{GCD}(10 \times [1 \cdot r])$ , and GCD represents the function of the greatest common divisor. Secondly, according to the MSDS working speed and the influence of proportional coefficient on critical speeds of the system, appropriate proportional coefficient is suggested to keep critical speeds away from working speeds. Additionally, selecting a larger derivative coefficient to increase the equivalent damping of AMBs can effectively attenuate the vibration of MSDS, but it should be noted that when equivalent damping is too large, it will increase the instability risk by directly amplifying the noise in the derivative signal. Thirdly, the designed operating speed of MSDS should be far away from critical speeds corresponding to the bending modes.

#### 4. Conclusions

In this paper, a dynamic model is established to investigate the influence of speed ratio on nonlinear dynamics of MSDS with fixed-point rubbing. The nonlinear support characteristics of AMBs are modeled by the equivalent magnetic circuit method; the Lankarani-Nikravesh model is adopted to describe the impact force, and the dynamic model established by the finite element method and solved by the Newmark- $\beta$  method. The nonlinear dynamic behaviors are discussed by bifurcation diagrams, trajectories, Poincaré maps and spectrum graphs, and the following conclusions are drawn.

(1) Speed ratio has a significant influence on the dynamic responses of MSDS. The fundamental sub-synchronous vibration of period  $n$  is determined by the speed ratio  $r$ ,

where  $n$  equals to the greatest common divisor of 10 times 1 and  $r$  divided by 10. For the sub-synchronous vibration of period  $mn$  ( $m = 1, 2, 3, \dots$ ), the minimum dimensionless frequency component is  $1/mn$  and other frequency components can be regularly expressed as integer multiples of the minimum dimensionless frequency component. The quasi-periodic vibration is characterized by  $mn$  closed curves in Poincaré maps. The main frequency components can be expressed as a variety of combined frequency components of the rotating frequency difference and its fractional frequency for quasi-periodic and chaotic vibrations.

(2) In order to reduce the severity of fluctuating stresses caused by non-synchronous vibrations, three methods are proposed. First, the speed ratio corresponding to smaller  $n$  is suggested. Second, appropriate control parameters are recommended to reduce vibration amplitudes or keep critical speeds away from operating speeds. Third, the operating speeds of MSDS should be far away from the critical speeds that correspond to the bending modes.

**Author Contributions:** D.W.: Conception of the study, propose theory and method, supervisor and conceptualization; S.C.: Software, writing and data curation; N.W.: Supervision and resources; J.Z.: Drawing and funding acquisition; B.W.: Project administration and resources. All authors have read and agreed to the published version of the manuscript.

**Funding:** This research was funded by the National Natural Science Foundation of China (51975427/52072116), the Natural Science Foundation Youth Project of Hubei Province (2022CFB917), the Scientific and Technology Research Project from Education Department of Hubei Province (D20221803), the Hubei Key Laboratory of Automotive Power Train and Electronic Control (ZDK1202103) and the Doctoral Scientific Research Starting Foundation of Hubei University of Automotive Technology (BK202009).

**Data Availability Statement:** The data used to support the findings of this study are available from the corresponding author upon request.

**Conflicts of Interest:** The authors declare no conflict of interest.

## References

- Hirst, M.; McLoughlin, A.; Norman, P.J.; Galloway, S.J. Demonstrating the more electric engine: A step towards the power optimized aircraft. *IET Electr. Power App.* **2011**, *5*, 3–13. [\[CrossRef\]](#)
- Yang, Y.; Cao, D.Q.; Wang, D.Y.; Jiang, J.Y. Fixed-point rubbing characteristic analysis of a dual-rotor system based on the Lankarani-Nikravesh model. *Mech. Mach. Theory* **2016**, *103*, 202–221. [\[CrossRef\]](#)
- Jin, Y.L.; Liu, Z.W.; Chen, Y.S. Simulation of blade-casing rubbing for a dual-rotor system of an aero-engine. *Acta Aeronaut. Astronaut. Sin.* **2022**, *43*, 498–511.
- Yu, P.C.; Chen, G.; Li, L.X. Modal analysis strategy and nonlinear dynamic characteristics of complicated aero-engine dual-rotor system with rub-impact. *Chin. J. Aeronaut.* **2022**, *35*, 184–203. [\[CrossRef\]](#)
- Yu, P.C.; Li, H.; Wang, C.; Chen, G. Insights into the nonlinear behaviors of dual-rotor systems with inter-shaft rub-impact under co-rotation and counter-rotation conditions. *Int. J. Nonlin. Mech.* **2022**, *140*, 103901. [\[CrossRef\]](#)
- Lin, W.H.; Wang, C. Nonlinear Dynamics of Dual-Rotor System in Aero-engine under Rub-Impact Between Shafts. *J. Propuls Technol.* **2023**, *1*, 1–14.
- Yang, Y.; Cao, D.Q.; Yu, T.H.; Wang, D.Y.; Li, C.G. Prediction of dynamic characteristics of a dual-rotor system with fixed point rubbing—Theoretical analysis and experimental study. *Int. J. Mech. Sci.* **2016**, *115–116*, 253–261. [\[CrossRef\]](#)
- Wang, N.F.; Liu, C.; Jiang, D.X.; Behdinan, K. Casing vibration response prediction of dual-rotor-blade-casing system with blade-casing rubbing. *Mech. Syst. Signal Process.* **2019**, *118*, 61–77. [\[CrossRef\]](#)
- Chen, Y.; Hou, L.; Chen, G.; Song, H.Y.; Lin, R.Z.; Jin, Y.H. Nonlinear dynamics analysis of a dual-rotor-bearing-casing system based on a modified HB-AFT method. *Mech. Syst. Signal Process.* **2023**, *185*, 109805. [\[CrossRef\]](#)
- Zhang, T.C.; Cao, S.Q.; Li, L.Q.; Guo, H.L. Analysis and experiment of coupled bending and torsional vibration of a rub-impact dual-rotor system. *J. Aerosp. Power* **2019**, *34*, 643–655.
- Ebrahimi, R.; Ghayour, M.; Khanlo, H. Effects of some design parameters on bifurcation behavior of a magnetically supported coaxial rotor in auxiliary bearings. *Eng. Comput.* **2017**, *34*, 2379–2395. [\[CrossRef\]](#)
- Ebrahimi, R.; Ghayour, M.; Khanlo, H. Chaotic vibration analysis of a coaxial rotor system in active magnetic bearings and contact with auxiliary bearings. *J. Comput. Nonlinear Dyn.* **2017**, *12*, 031012. [\[CrossRef\]](#)
- Wang, D.X.; Wang, N.X.; Chen, K.S.; Ye, C. Dynamic characteristics of magnetic suspended dual-rotor system by Riccati transfer matrix method. *Shock Vib.* **2019**, *4*, 9843732. [\[CrossRef\]](#)

14. Wang, D.X.; Wang, N.X.; Chen, K.S. Unbalance response of a magnetic suspended dual-rotor system. *Proc. Inst. Mech. Eng. Part G J. Aerosp. Eng.* **2019**, *233*, 5758–5772. [[CrossRef](#)]
15. Wang, N.X.; Liu, M.Z.; Yao, J.F.; Ge, P.P.; Wu, H.C. Numerical study on unbalance response of dual-rotor system based on nonlinear bearing characteristics of active magnetic bearings. *Actuators*. **2023**, *12*, 86. [[CrossRef](#)]
16. Wang, D.X.; Wang, N.X.; Chen, K.S. Fixed-point rubbing characteristics of magnetic suspended dual-rotor system. *China Mech. Eng.* **2021**, *32*, 1686–1699.
17. Wang, D.X.; Yi, T.; Qin, X.; Zhang, J.; Yin, C.C.; Wang, B.H. Research on vibration characteristic analysis of magnetic suspended dual-rotor system with fixed-point rubbing. *Shock Vib.* **2022**, *2022*, 9254013. [[CrossRef](#)]
18. Zhang, G.; Xi, G. Vibration control of a time-delayed rotor-active magnetic bearing system by time-varying stiffness. *Int. J. Appl. Mech.* **2022**, *14*, 2250007. [[CrossRef](#)]
19. Jiang, K.J.; Zhu, C.S.; Chen, L.L.; Qiao, X.L. Multi-DOF rotor model based measurement of stiffness and damping for active magnetic bearing using multi-frequency excitation. *Mech. Syst. Signal Process.* **2015**, *60*, 358–374. [[CrossRef](#)]
20. Inayat-Hussain, J.I. Nonlinear dynamics of a magnetically supported rigid rotor in auxiliary bearings. *Mech. Mach. Theory* **2010**, *45*, 1651–1667.
21. Inayat-Hussain, J.I. Nonlinear dynamics of a statically misaligned flexible rotor in active magnetic bearings. *Commun. Nonlinear Sci.* **2010**, *15*, 764–777.
22. Inayat-Hussain, J.I. Geometric coupling effects on the bifurcations of a flexible rotor response in active magnetic bearings. *Chaos Solitons Fractals* **2009**, *41*, 2664–2671. [[CrossRef](#)]
23. Wang, Z.B.; Mao, C.; Zhu, C.S. A design method of PID controllers for active magnetic bearings-rigid rotor systems. *Proc. CSEE* **2017**, *38*, 6154–6163.

**Disclaimer/Publisher’s Note:** The statements, opinions and data contained in all publications are solely those of the individual author(s) and contributor(s) and not of MDPI and/or the editor(s). MDPI and/or the editor(s) disclaim responsibility for any injury to people or property resulting from any ideas, methods, instructions or products referred to in the content.